Galaxy gas as obscurer: I. GRBs x-ray galaxies and find a $N_{\rm H}^3 \propto M_\star$ relation

Johannes Buchner[1,2]⋆, Steve Schulze[2,1], Franz E. Bauer[2,1,3]

[1]*Millenium Institute of Astrophysics, Vicuña Mackenna 4860, 7820436 Macul, Santiago, Chile*
[2]*Pontificia Universidad Católica de Chile, Instituto de Astrofísica, Vicuña Mackenna 4860, 7820436 Macul, Santiago, Chile*
[3]*Space Science Institute, 4750 Walnut Street, Suite 205, Boulder, Colorado 80301*

ABSTRACT

An important constraint for galaxy evolution models is how much gas resides in galaxies, in particular at the peak of star formation $z = 1 - 3$. We attempt a novel approach by letting long-duration Gamma Ray Bursts (LGRBs) x-ray their host galaxies and deliver column densities to us. This requires a good understanding of the obscurer and biases introduced by incomplete follow-up observations. We analyse the X-ray afterglow of all 844 *Swift* LGRBs to date for their column density $N_{\rm H}$. To derive the population properties we propagate all uncertainties in a consistent Bayesian methodology. The $N_{\rm H}$ distribution covers the $10^{20-23} {\rm cm}^{-2}$ range and shows no evolutionary effect. Higher obscurations, e.g. Compton-thick columns, could have been detected but are not observed. The $N_{\rm H}$ distribution is consistent with sources randomly populating a ellipsoidal gas cloud of major axis $N_{\rm H}^{\rm major} = 10^{23} {\rm cm}^{-2}$ with 0.22 dex intrinsic scatter between objects. The unbiased SHOALS survey of afterglows and hosts allows us to constrain the relation between *Spitzer*-derived stellar masses and X-ray derived column densities $N_{\rm H}$. We find a well-constrained powerlaw relation of $N_{\rm H} = 10^{21.7} {\rm cm}^{-2} \times \left(M_\star / 10^{9.5} M_\odot \right)^{1/3}$, with 0.5 dex intrinsic scatter between objects. The Milky Way and the Magellanic clouds also follow this relation. From the geometry of the obscurer, its stellar mass dependence and comparison with local galaxies we conclude that **LGRBs are primarily obscured by galaxy-scale gas**. Ray tracing of simulated *Illustris* galaxies reveals a relation of the same normalisation, but a steeper stellar-mass dependence and mild redshift evolution. Our new approach provides valuable insight into the gas residing in high-redshift galaxies.

Key words: Keywords: gamma-ray burst: general – galaxies: general – X-rays: galaxies – galaxies: structure – galaxies: ISM – X-rays: ISM – Magellanic Clouds – dust, extinction

1 INTRODUCTION

Galaxies radiate because of gas condensed into stars and accretion onto compact objects. Reconciling that emission with the gas actually present in galaxies is important to understand processes of galaxy evolution, including the efficiency of star formation and accretion processes and the in-fall of cosmological gas into galaxy halos. Most interesting are constraints at the peak of star formation ($z = 1 - 3$, Madau & Dickinson 2014) and at the peak of the accretion history ($z = 0.5 - 3$, Aird et al. 2010; Ueda et al. 2014; Buchner et al. 2015; Aird et al. 2015). At that time, the gas content in galaxies was probably higher, as indicated by molecular gas measurements (e.g. Tacconi et al. 2013), the current primary tracer of galaxy gas at high redshifts.

The gas in galaxies in turn can attenuate the radiation by absorption along the line of sight (LOS). This allows one to con-

strain some properties of the galaxy gas (e.g., reddening in the UV; Boquien et al. 2013). Because only the total LOS absorbing column can be measured, it remains unclear in individual galaxies at which scales the absorption is acting, and thus its density remains undetermined. The alternative is to find a statistical average over many sight-lines which probe galaxies under random viewing angles. A further challenge is that the underlying sources must be detected even in galaxies with the largest gas contents, and the measurement for absorption must remain sensitive at high column densities.

This work uses Gamma Ray Bursts (GRBs) as beacons inside high-redshift (primarily $z = 0.5 - 3$) galaxies to estimate the importance of galaxy-scale gas obscuration. Long-duration GRBs (LGRBs, duration > 2s) are thought to be caused by the death of massive stars (Woosley & Bloom 2006; Hjorth & Bloom 2012), and thus approximately trace star formation but with a bias towards metal-poor galaxies (see Krühler 2015; Perley et al. 2016a, for recent reviews). LGRB detection via their prompt gamma ray emission avoids detection biases due to absorption. The afterglow of

⋆ E-mail: johannes.buchner.acad@gmx.com

LGRBs emits X-rays which can be used to assess the column density through photo-electric absorption, primarily from electrons in O and Fe atoms along the LOS[1]. This work uses the distribution of LOS column densities to reconstruct the galactic gas of GRB host galaxies at high redshift.

Three major methodological contributions lead up to this work: 1) The launch of the *Swift* satellite (Gehrels 2004) resulted in a wealth of GRB data with accurate positioning and timely afterglow spectroscopy. A series of papers by Campana and collaborators already exploited these data using best-fit column densities (Campana et al. 2006, 2010a, 2012). 2) By 2012 it was appreciated that current redshift determination practices introduce systematic sample biases that tend to exclude dusty, massive host galaxies, potentially under-estimating the entire column density distribution of the GRB population (see e.g. Fynbo et al. 2009; Krühler et al. 2011; Perley et al. 2013). This work thus also investigates the nature of that bias (see also Campana et al. 2012, for a bright sample analysis). 3) Reichart (2001) and Reichart & Price (2002) developed a hierarchical Bayesian inference framework for GRB population analysis which incorporates the uncertainties of each individual X-ray spectral analysis. We use this framework to also consistently include GRBs without redshift information, and provide a more advanced statistical analysis for potential redshift evolution of the GRB population.

This work begins with describing the statistical framework in Section 2. We describe the LGRB samples used in this work, the data reduction and spectral analysis procedures in Section 3. Section 4 presents the results of the spectral analysis and population properties. There we begin with empirical models and in turn investigate more physical models, redshift evolution, host mass dependence and the effect of redshift-incomplete samples. We discuss our results in Section 5, putting our results in the context of previous investigation of LGRB obscurers (5.2) and comparing our results to local galaxies. Finally we look inside simulated galaxies to investigate their gas columns (Section 5.5) before summarising our conclusions in Section 6.

2   METHODOLOGY

To analyse the GRB population we consider several parameterised models. Each model M predicts the distribution of column densities, $p(N_H|M, \theta)$, between the GRB and the observer. The parameters θ of each model are constrained with X-ray spectral data of a GRB sample, described in the next section, which is a (Poisson) draw from the general GRB population. We define the likelihood of observing data D for n objects as

$$\mathcal{L}_M(\theta) = \prod_{i=1}^{n} \boxed{+} \, p(D_i|N_H, \phi_i) \cdot p(N_H, \phi_i|M, \theta) \, d\log N_H d\phi_i, \quad (1)$$

where $p(D_i|\cdot)$ is the likelihood of object i to have column density N_H and other properties ϕ_i relevant for the X-ray spectrum, such as redshift and the photon index Γ (see below in Section 3.3). That likelihood $p(D_i|\cdot)$ is discussed in more detail Section 3.3, but briefly speaking it is a Poisson likelihood due to the count nature of X-ray photon detections. The sample and its X-ray data are discussed in the section below.

The distribution of properties within the population is described by the $p(N_H, \phi|M, \theta)$, which is the product of the column density distribution $p(\log N_H|M, \theta)$, the photon index distribution and further distributions assumed for the remaining spectral parameters (defined below). The photon index distribution is assumed to be Gaussian, with the mean and standard deviation free parameters in θ and determined simultaneously. Models for the column density distribution, which are focus of this paper, $p(N_H|M, \theta)$ are presented in Section 4.1.

To illustrate the meaning of Equation 1 consider the case of objects with no information, i.e., a flat $p(D_i|N_H)$. Any population model $p(\log N_H)$ is then equally probable, including delta functions that predict a constant N_H for all objects. This follows from $p(\log N_H)$ being normalised in $\log N_H$ space. In contrast, if an object has a well-constrained likelihood $p(D_i|N_H)$, the integral will be maximised by population models with some probability there. If two objects have well-constrained, but mutually exclusive N_H constraints, then the population model $p(\log N_H)$ has to distribute its probability weight, thereby representing scatter in the population. Objects without data constraints are effectively "wildcards": their integral mass is concentrated wherever the specific population model $p(\log N_H)$ is concentrated, creating degenerate solutions of equal likelihood $\mathcal{L}$.

Equation 1 defines the likelihood which can be explored with maximum likelihood methods or a Bayesian approach by varying the population model parameters θ. This likelihood is well-known in luminosity function works (e.g., Marshall et al. 1983; Loredo 2004; Kelly et al. 2008[2]) and has also been used in previous studies of the column density of GRBs (Reichart 2001; Reichart & Price 2002). To compare various models, the Akaike information criterion (AIC; Akaike 1974) is adopted. The AIC prefers the model with the highest maximum likelihood $\mathcal{L}_M(\theta_{max})$, but punishes by the number of parameters m according to AIC $:= 2 \cdot \mathcal{L}_M(\theta_{max}) - 2 \cdot m$ (higher AIC is better).

3   DATA

3.1   Sample Selection

The *Swift* satellite (Gehrels 2004) is a dedicated GRB mission which features on-board detection of GRBs with a wide field γ-ray detector and automatic followup using X-ray and optical/UV telescopes for determining the source position to arcsec accuracy. We analysed the X-ray spectrum of all GRBs in the *Swift* Burst Analyser (Evans et al. 2010) archive[3] up to June 24th, 2015. Our parent sample is 920 GRBs detected by *Swift*.

This work ultimately aims to constrain the intrinsic column density distribution of GRB host galaxies. We select all detected long-duration GRB, which are associated with the death of massive stars, and therefore can be expected to trace the galactic gas content through star formation. To illustrate our sample selection, Figure 1 shows the distribution of all *Swift*-detected GRBs on the sky. The positions of GRBs are constrained on-board by combining the gamma-ray, X-ray and optical/UV telescopes. Bursts of short duration (green star symbols, $T_{90} < 2s$) were excluded. These have been identified through mentions of short duration in associated GRB Coordinates Network (GCN) Circulars. This leaves 844 LGRBs,

---

[1] The alternative hypothesis of a He-dominated, ionised absorber (Watson et al. 2013) is discussed extensively in Section 5.4.

[2] See the Appendix of Buchner et al. 2015 for a derivation and how intermediate priors are handled.

[3] http://www.swift.ac.uk/
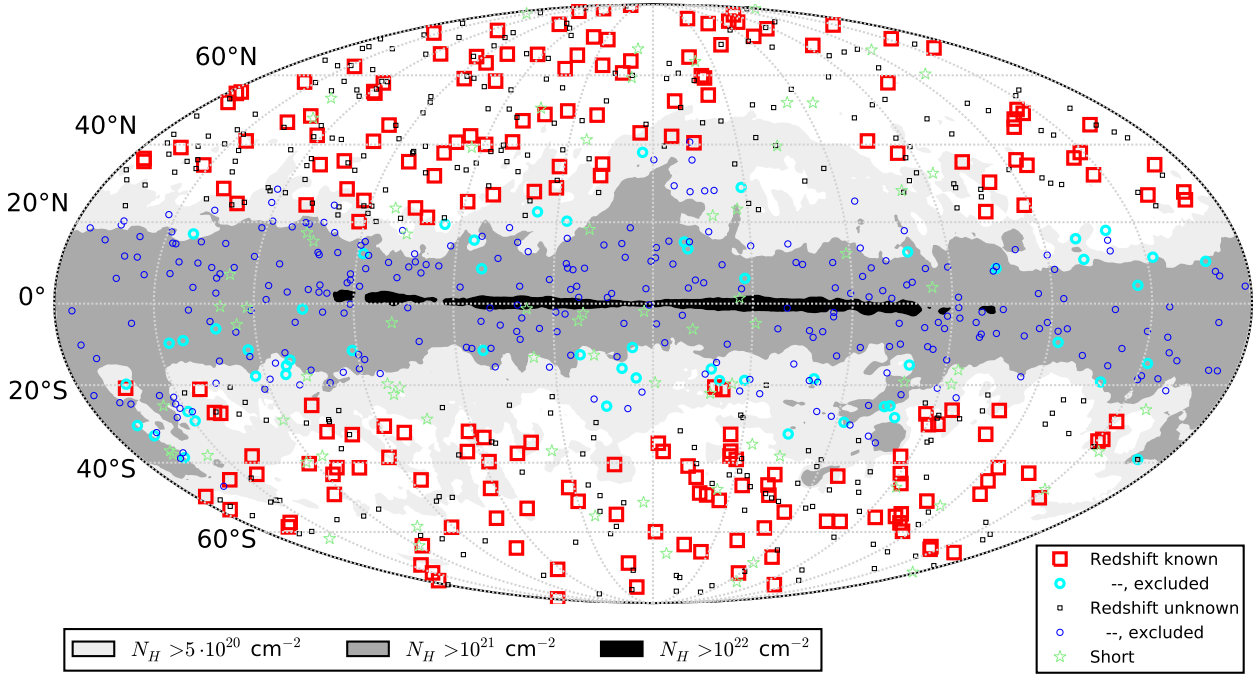
Figure 1. Distribution of the GRB sample in Galactic coordinates (points). To avoid Galactic absorption the Galactic latitude $|b| < 20°$ and regions with $N_H > 10^{21}$cm^{-2} are excluded from the sample (circles). A smoothened Galactic column density map is shown in the background (Kalberla et al. 2005).

Table 1. Sample selection.

Sample name	Parent sample	Size	Criteria
Swift	http://www.swift.ac.uk/, including non-detected afterglows	920	*Swift*-detected GRBs
Long	Swift	844	$T_{90} > 2$
Complete sample	Long	512	$N_H^{MW} < 10^{21}$cm^{-2} and $|b| > 20°$.
Redshift subsample	Complete sample	163	redshift known and $z = 0.3 - 3.2$
SHOALS	-	119	Perley et al. (2016b)
unbiased sample	SHOALS	119	$N_H^{MW} < 10^{21}$cm^{-2} and $|b| < 20°$.
High-mass subsample	unbiased sample	25	*Spitzer* 3.6μm band < -22 mag
Low-mass subsample	unbiased sample	94	*Spitzer* 3.6μm band > -22 mag, or uncertain
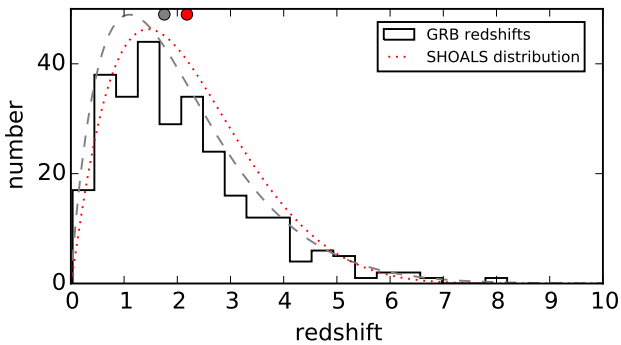
Figure 2. Redshift distribution. The histogram of redshifts is shown in black. The grey dotted line indicates a fitted Beta distribution. The red dotted line shows the redshift distribution of the SHOALS unbiased sample, which peaks at slightly higher redshifts (filled circles indicate the respective medians). Most LGRBs are found in the redshift interval $z = 0.5 - 3$.

indicated as squares and circles in Figure 1. Regions where the Milky Way contributes substantial column densities (over-plotted shades) have to be excluded. We exclude positions with Galactic column densities $N_H^{MW} > 10^{21}$cm^{-2} and Galactic latitudes $|b| < 20°$. We call this sample with 512 objects the *complete sample* (see Table 1) as it is unbiased against obscuration.

The availability of redshift information is important to constrain the obscuring column density from the X-ray spectrum. For 208 LGRBs, redshifts have been determined previously and are indicated by red squares in Figure 1. Those 163 objects with redshifts in the range $z = 0.3 - 3.2$ are called the *redshift subsample* (see Table 1). This criterion excludes very high-redshift afterglows for which the imprint of absorption is not observable, and low-luminosity LGRBs at low redshifts which may have different progenitors or emission mechanisms (see Dereli et al. 2015, and references therein).

Whether a redshift has been successfully determined for a particular LGRB depends on many factors and thus the LGRBs with available redshifts constitute a biased subsample, showing higher fluxes, lower absorption than carefully constructed samples with dedicated follow-up (Fynbo et al. 2009). Working with unbiased samples is thus important to determine the underlying distribution (e.g. Campana et al. 2012). Such samples are pre-selected by

GRB position relative to the Sun, Moon, galactic plane and available observatories, but importantly not by afterglow detection or magnitude. The sample is then followed up with deep ground-based observations to determine redshifts and host properties (e.g. Jakobsson et al. 2006a; Fynbo et al. 2009; Greiner et al. 2011; Krühler et al. 2012; Jakobsson et al. 2012; Schulze et al. 2015; Perley et al. 2016b). The largest unbiased sample to date is the *Swift* Gamma-Ray Burst Host Galaxy Legacy Survey (SHOALS, Perley et al. 2016b). Their redshift distribution is depicted in Figure 2 as a red dotted line. In comparison, the redshift distribution of the complete sample, where redshifts are available, peaks at lower redshifts than the redshift subsample (black histogram).

To overcome the biases of redshift selection, two approaches are followed: (a) The entire sample is used, including objects without determined redshift. This sample does then not have a redshift selection bias, but has low redshift completeness ($\sim 40\%$). The distribution in the sky of this sample is shown in Figure 1 with square symbols. (b) The SHOALS sample is adopted with the same Milky Way absorption criteria. The resulting 105 objects form an *unbiased sample* with $\sim 90\%$ redshift completeness. For objects with known spectroscopic redshift we fix the redshift during spectral analysis, for objects without redshifts or photometric redshifts we adopt as a redshift prior the unbiased distribution of SHOALS.

Perley et al. (2016c) investigated the masses of GRB host galaxies. They obtained *Spitzer* follow-up observations of the SHOALS sample in the $3.6\mu m$ band, where -22 mag corresponds approximately to a stellar mass of $10^{10} M_{\odot}$. We split our *unbiased sample* further into *low-mass* and *high-mass subsamples* using this criterion (see Table 1). These subsamples have 94 and 25 objects, respectively.

3.2 Data reduction

X-ray observations were taken using the XRT instrument on-board *Swift* (Burrows et al. 2005) which is sensitive in the $0.2-10$ keV energy range. To minimise pile-up, XRT is operated in Window Timing (WT) mode for high-flux GRB afterglows. Otherwise, Photon Counting mode (PC) is used. GRBs show strong evolution in their light curve and spectral hardness. This work focuses on the emission of the X-ray afterglow, which is assumed here to be intrinsically a powerlaw, and to have a time-invariant spectral shape. However, the early evolution of an afterglow ($t \lesssim 1000$ s) can be affected by prompt emission. This phase can be easily identified by its rapid decay ($t^{-\alpha}$ with $\alpha > 2$) and spectral softening. For this we turn to the Swift Burst Analyser, which analyses the light curve as described in Evans et al. (2009). Briefly speaking, the light curve is approximated by piece-wise powerlaw evolutions. We discard the initial two time intervals if either show a powerlaw decline with a slope steeper than -2, and any immediately following intervals that also abide by this criterion. Flare intervals are also discarded. The remaining time segmentation was checked and corrected by individually inspecting each light curve and hardness ratio. The final time segmentation is listed for each source in the catalogue released with this paper (see below).

The spectra from the chosen time segmentation was then extracted using the Swift Burst Analyser, which automatically screens event files, selects appropriate energy ranges, applies grade filtering, and chooses spectral extraction regions to avoid pile-up while maximising S/N. Background spectra were extracted from appropriate surrounding areas. Ancillary Response Files (ARFs) and Response Matrix Files (RMFs) were computed. The $0.5 - 5$ keV data

were used in the spectral analysis below, as XRT is most sensitive there with the background well-behaved and sub-dominant.

Because XRT automatically observes bright sources in WT mode, but faint sources and late-time observations in PC mode, two data sets may be available for any GRB. For the majority of GRBs, WT mode is not or only very briefly used. Brief WT observations were not analysed here as it is difficult to constrain the background and in practice they do not improve constraints over the PC mode observations. The criterion for including WT spectra was that the background spectrum must contain more than 150 counts. The PC mode data are always used, if available.

In some cases, no time interval can be safely used. This can occur if only the prompt emission is bright enough to be detected. Furthermore there are sources with no detected afterglow[4]. These sources lacking X-ray data were included (if *Swift*-triggered) in our analysis nevertheless, as they could be heavily obscured, and comprise part of the unbiased sample.

3.3 X-ray spectral analysis

The intrinsic afterglow spectrum is thought to be due to synchrotron radiation (Piran 2005). We model the relevant portion for the $0.5 - 5$ keV energy range as a power law $\phi(E) = A \times E^{-\Gamma}$, which is then photo-electrically absorbed: once by an intrinsic absorption within the host galaxy $N_{\rm H}$ (see below), and once with a Galactic absorption $N_{\rm H}^{\rm MW}$ using the TBABS ISM absorption model (Wilms et al. 2000, with cross-sections from Verner et al. 1996). The source model parameters are thus the normalisation A, the photon index Γ, and the absorbing column densities $N_{\rm H}$ and $N_{\rm H}^{\rm MW}$. The intrinsic power law is assumed to remain constant with time: hardness ratio variations where not found (see above) and luminosity variations do not affect the Poisson fit when we are only interested in the spectral shape. The background spectrum is empirically modelled as described in Appendix B.

Towards Compton-thick densities, here $N_{\rm H} > 10^{24} {\rm cm}^{-2}$ for simplicity, effects beyond photo-electric absorption become important. Such columns in a dense GRB environment or host galaxy gas could block even the X-ray afterglow emission. Therefore we search for evidence of high column densities. We adopt the SPHERE model of Brightman & Nandra (2011), which describes photo-electric absorption, Compton-scattering and line fluorescence computed self-consistently in a spherical, constant-density obscurer geometry with a powerlaw source in the centre. The SPHERE model supports column densities up to $N_{\rm H} = 10^{26} {\rm cm}^{-2}$. Solar metallicities (Anders & Ebihara 1982) are assumed when deriving the neutral hydrogen-equivalent column densities $N_{\rm H}$. However, LGRBs appear to be often found in low-metallicity environments (Graham & Fruchter 2013). Derived column densities should thus be primarily considered as metal column densities as relevant for photo-electric absorption of X-rays. We also repeated our entire analysis using the spectral analysis the TBABS ISM absorption model (Wilms et al. 2000, with cross-sections from Verner et al. 1996) and find consistent column densities within the uncertainties. However, in high-obscuration sources ($N_{\rm H} \gtrsim 10^{22.5} {\rm cm}^{-2}$) TBABS (and other photo-absorption models) sometimes produces a secondary, Compton-thick solution of lower probability. This solution is not physical as it is not present when analysing with the more appropriate SPHERE model. We therefore use the SPHERE model throughout.

To obtain probability distributions for the column density $N_{\rm H}$,

---

[4] Listed separately on the http://www.swift.ac.uk/ website
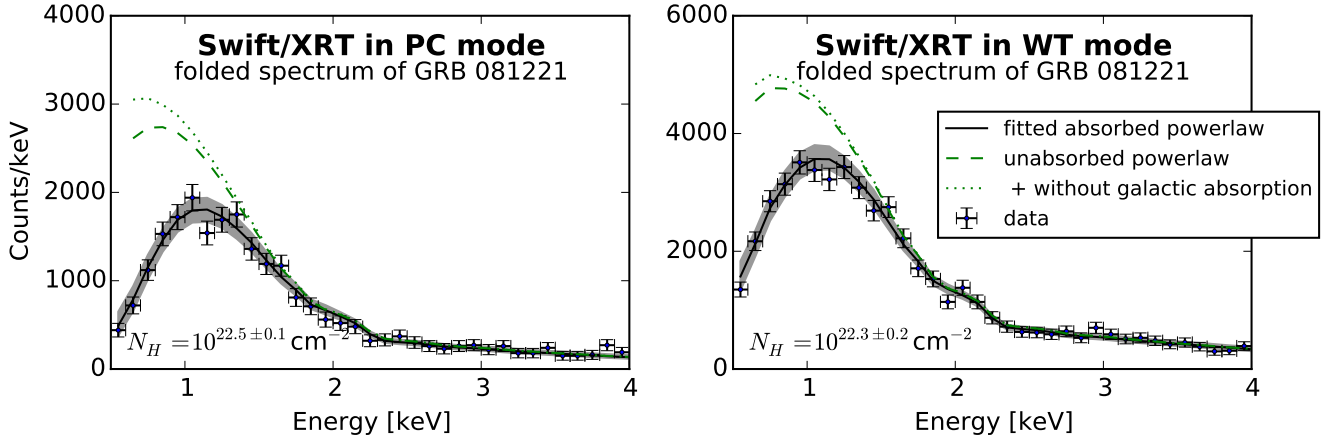
Figure 3. XRT convolved X-ray spectrum of GRB 081221. *Left*: PC mode spectrum. *Right*: WT mode spectrum. The absorbed powerlaw model (black line, with 3σ uncertainties in grey) fits the data (black error bars, binned for plotting) well. For this source, the column density is $N_H \approx 10^{22.5} \mathrm{cm}^{-2}$. The dashed green line indicates the fit of an unabsorbed powerlaw, which is clearly ruled out by the low number of counts at $0.5 - 1\,\mathrm{keV}$. The dotted line shows the effect if the Galactic absorption, $2 \times 10^{21} \mathrm{cm}^{-2}$ for this source, is also removed.

Table 2. Parameters of the spectral model and their priors.

Parameter	Symbol	Prior
Normalisation	A	log-uniform $10^{-10} - 10^{2} \mathrm{keV}^{-1} \mathrm{cm}^{-2} \mathrm{s}^{-1}$
Powerlaw Slope	Γ	uniform $1 - 3$
Column density (intrinsic)	N_H	log-uniform $10^{19} - 10^{26} \mathrm{cm}^{-2}$
Galactic column density	N_H^{MW}	log-normal around LAB value; standard deviation $\frac{1}{3} \ln 3$
Redshift	z	fixed if spectroscopy available; otherwise SHOALS distribution (Figure 2)

a Bayesian methodology is adopted for analysing the X-ray spectrum (van Dyk et al. 2001; Buchner et al. 2014). The Bayesian X-ray Analysis (BXA) software, which connects the Sherpa X-ray spectral analysis tool (Freeman et al. 2001) to the MultiNest algorithm (Feroz et al. 2009, 2013), is used with a Poisson likelihood (Cash 1979). This methodology has the benefit of exploring the full parameter space and propagating correlated uncertainties, e.g., between redshift, obscuring column and the powerlaw slope.

The Bayesian approach requires the explicit specification of priors. They are listed for each parameter separately in Table 2. For the Galactic column density N_H^{MW}, a informative normal prior is adopted around the value measured by the Leiden/Argentine/Bonn (LAB) Survey of Galactic HI (Kalberla et al. 2005) at the source position. This estimate may be slightly off in unfortunate conditions, if the Galactic gas is very structured and/or the position is not precisely known. This uncertainty is allowed by putting a Gaussian prior around $\log N_H^{\mathrm{MW}}$ with a standard deviation of $\sigma = \frac{1}{3} \log 3$, i.e., allowing a three sigma deviation of a factor of 3 in N_H^{MW}. This only broadens our uncertainties in N_H, especially when $N_H^{\mathrm{MW}} \approx N_H$. The uninformative priors adopted for N_H and Γ are later replaced by the populations' column density distribution and thus do not influence the results. For completeness, we include GRBs without redshift information. For these we adopt as a redshift prior the distribution of the SHOALS sample (see Figure 2, red dotted line), which encodes the assumption that these GRBs stem from the same underlying distribution. Perley et al. (2016b) tested the influence of their fluence cut on the redshift distribution and found it to be negligible.

Figure 3 shows an example of a fitted X-ray spectrum in both PC and WT mode of a highly obscured GRB. None of the objects show contradictory constraints between the two modes, which could occur due to poor fits of the source or background spectrum. As we have analysed the WT and PC mode spectra separately, no assumptions about the two spectra having the same luminosity or photon index are made. Finally, the constraints for column density N_H from the WT and PC mode spectra are merged (if both available) by multiplying the PC mode probability distributions (in N_H and Γ) by the WT N_H probability distribution, thus tightening the constraints on N_H. The photon index Γ can show degeneracies with N_H in low-count spectra, so its probability distribution is carried along as described in Section 2. The population distributions of Γ, N_H and z are constrained simultaneously. The photon index distribution is reported in Appendix A.

4 RESULTS

Before inferring the population properties of GRB obscurers, we briefly describe the spectral analysis results of the sample. Their distribution in column density and redshift is shown in Figure 4 for the redshift subsample at $z = 0.3 - 3.2$. Out of the 163 objects, 28 can be securely identified as intrinsically obscured ($N_H > 10^{22} \mathrm{cm}^{-2}$ with 90% probability), and four can be securely identified as intrinsically unobscured ($N_H < 10^{21} \mathrm{cm}^{-2}$ with 90% probability). GRB 080207 shows the highest obscuration with $N_H \approx 10^{23} \mathrm{cm}^{-2}$. In the complete sample, which comprises all LGRB detections of *Swift*, all sources with X-ray data are constrained to $N_H < 2 \times 10^{23} \mathrm{cm}^{-2}$. A large portion of the sample only has upper limits for the column density distribution. The lowest upper limit is $N_H < 10^{20.54} \mathrm{cm}^{-2}$ (90% quantile) in GRB 061021. A catalogue of the sample analysis results of all GRBs is released with this paper. Its columns are described in Table 3.

To test whether we might have missed any heavily obscured (dark) LGRB, we simulate PC mode spectra for all sources with $z = 1 - 3$, focusing on the bulk of the sample redshift distribution. We use the same spectral parameters (normalisation, photon index) but set the obscuring column to $N_H = 10^{24} \mathrm{cm}^{-2}$. This reduces the median number of detected counts in the $0.5 - 5 \mathrm{keV}$ range from

Name	Duration	RA	Dec	b[°]	N_H^{MW}	z	Time selection[s]	N_H	$N_{H,10\%}$	$N_{H,90\%}$
GRB 041218	-1	01:39:07	+71:20:29	8.8	4.17×10^{21}	0	19350-20616	8.55×10^{20}	1.85×10^{19}	5.30×10^{22}
GRB 061021	46.2	09:40:36	-21:57:05	22.6	5.53×10^{20}	0.3463	367-4384111	2.01×10^{20}	1.09×10^{20}	4.92×10^{20}
GRB 061021	46.2	09:40:36	-21:57:05	22.6	5.53×10^{20}	0.3463	367-4384111	2.01×10^{20}	1.09×10^{20}	4.92×10^{20}
GRB 080207	340	13:50:03	+07:30:08	66.0	2.11×10^{20}	2858	130-324571	1.06×10^{23}	8.97×10^{22}	1.24×10^{23}
GRB 150616A	599.5	20:58:52	-53:23:38	-40.3	3.38×10^{20}	0	7635-312789	2.69×10^{22}	9.98×10^{21}	1.00×10^{23}
...										

Table 3. Catalogue (excerpt). Columns: (1) Name. (2) Duration (-1 indicates unknown). (3) Right ascension (J2000) in degrees. (4). Declination (J2000) in degrees. (5) Galactic latitude in degrees. (6) Galactic absorption in 10^{20}cm^{-2}. (7) Redshift (0 indicates unknown). (8) Time selection (in seconds since trigger) from which the afterglow emission was analysed in X-ray. If "n/a", no interval could be used. If not *Swift* triggered, this is also noted in this column. (9-12) Derived column density distribution from the X-ray spectrum analysis, listing (9) the mean in logarithmic units of cm^{-2}, (10) the 10% quantile and (11) the 90% quantile. This catalogue excerpt contains only the first and last GRB of our sample, as well as the lowest and highest obscuration GRBs found.
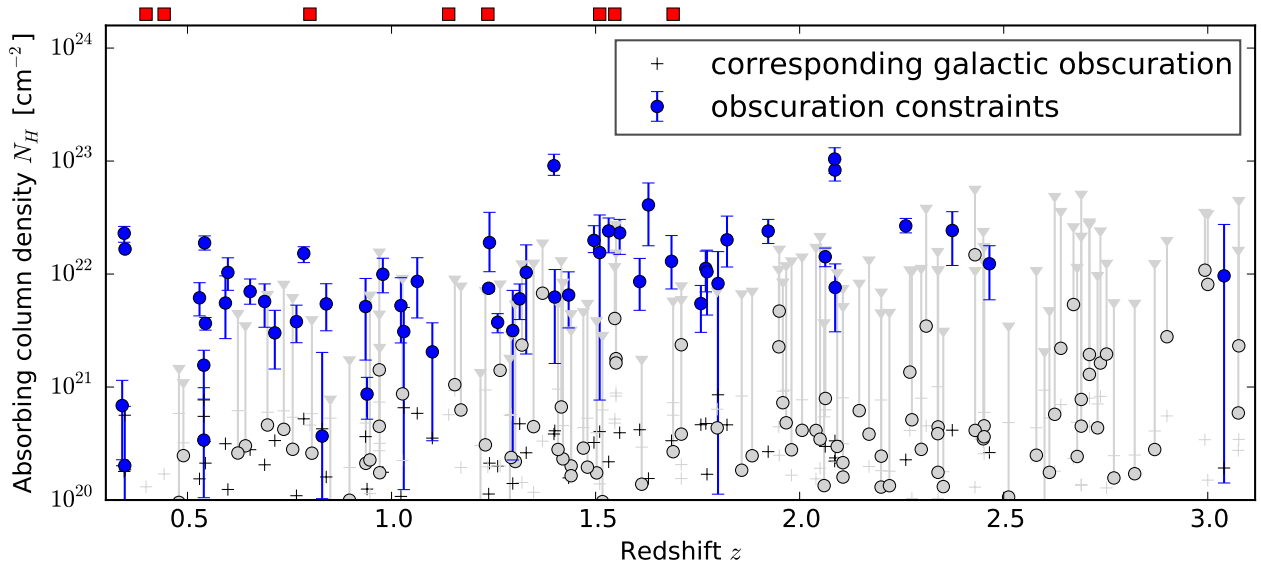
Figure 4. Redshift z and column density N_H distributions of the redshift subsample. Blue circles with error bars show objects with upper and lower limits; the circle indicates the posterior median, while the error bars show the 90% posterior probability quantiles. The black crosses show the Galactic column density corresponding to each object. Grey circles and crosses show the same, but for unobscured GRBs which only have upper limits. The red squares at the top indicate GRBs where no X-ray information is available, either because no afterglow was detected or no time intervals are free of prompt emission and flares. They are placed here at an arbitrarily for visualisation, but in the population analysis all N_H values are considered possible for these sources.

10266 (of which 2 are expected to be background counts) to 66 counts. Therefore there would still be enough contrast to detect and characterise the X-ray emission of such heavily obscured sources via their extremely hard spectra, which at these redshifts exposes the FeKα feature and the low-energy end of the Compton-hump.

4.1 Empirical Population Models

To analyse the population properties, specifically the obscurer column density distribution (CDD), models are adopted which predict the CDD. To start, we simply want to visualise the data constraints, which contain large uncertainties and upper limits (shown before in Figure 4).

Figure 5 shows the CDD fitted with several models. The points with error bars are derived by adopting 11 bins (the last bin extends up to 10^{26}cm^{-2}). We find that the column densities are confined to the $10^{20.5-23}$cm^{-2} range. Two models have been adopted in the literature to describe the CDD empirically, and are shown in Figure 5. Reichart & Price (2002) and Campana et al. (2010a) define a

broken powerlaw model (dashed line fit) as[5]

$$p(N_H|M_{BKNPL}, a, b, c) = \ln(10) \cdot \frac{b \cdot c}{c - b} \cdot \begin{cases} (N_H/a)^b & \text{if } N_H \leq a \\ (N_H/a)^c & \text{if } N_H > a \end{cases}. \quad (2)$$

The parameters b and c give the powerlaw slopes at the low and high-obscuration ends respectively, separated at the break a. Alternatively, a Gaussian distribution of log N_H (solid line fit in Figure 5) has been used (e.g. Campana et al. 2010a, 2012)

$$p(N_H|M_{GAUSS}, \mu, \sigma) = \frac{1}{\sqrt{2\pi}\sigma} \cdot \exp\left[-\frac{(\log N_H - \mu)^2}{2\sigma^2}\right]. \quad (3)$$

The parameters are the centre of the distribution μ and its width σ.

The constrained parameter values for the two models are listed in Table 4. The parameters are constrained by sampling the posterior distribution using MultiNest (Feroz et al. 2009, 2013) through PyMultiNest (Buchner et al. 2014). Flat priors have been

---

[5] In previous works the normalising factor ln(10) is erroneously divided, which is important for model comparison.

Table 4. Empirical models for the column density distribution for the complete sample.

Model	Component	Parameters			N_{params}	ΔAIC
Broken powerlaw		Break N_H	Low N_H slope	High N_H slope	5	0.0
		$\log a = 21.87 \pm 0.06$	$b = 0.78 \pm 0.09$	$c = -1.39 \pm 0.16$		
Gaussians		Mean	Standard deviation		4	-2.3
		$\mu = 21.64 \pm 0.03$	$\sigma = 0.55 \pm 0.03$			
Broken Powerlaws, 5 redshift bins					17	7.2
		Break N_H	Low N_H slope	High N_H slope		
	$z < 0.3$	$\log a_1 = 20.67 \pm 0.25$	$b_1 = 2.44 \pm 1.13$	$c_1 = -2.35 \pm 1.14$		
	$z = 0.3 - 1$	$\log a_2 = 21.81 \pm 0.18$	$b_2 = 0.74 \pm 0.18$	$c_2 = -1.85 \pm 0.70$		
	$z = 1 - 2$	$\log a_3 = 21.83 \pm 0.09$	$b_3 = 1.02 \pm 0.22$	$c_3 = -1.24 \pm 0.18$		
	$z = 2 - 4$	$\log a_4 = 22.03 \pm 0.12$	$b_4 = 0.68 \pm 0.12$	$c_4 = -1.67 \pm 0.44$		
	$z > 4$	$\log a_5 = 21.05 \pm 0.61$	$b_5 = 2.19 \pm 1.15$	$c_5 = -1.48 \pm 1.16$		
Gaussians, 5 redshift bins					12	-13.9
		Mean	Standard deviation			
	$z < 0.3$	$\mu_1 = 20.55 \pm 0.16$	$\sigma_1 = 0.14 \pm 0.26$			
	$z = 0.3 - 1$	$\mu_2 = 21.42 \pm 0.09$	$\sigma_2 = 0.54 \pm 0.08$			
	$z = 1 - 2$	$\mu_3 = 21.77 \pm 0.05$	$\sigma_3 = 0.50 \pm 0.04$			
	$z = 2 - 4$	$\mu_4 = 21.63 \pm 0.10$	$\sigma_4 = 0.61 \pm 0.08$			
	$z > 4$	$\mu_5 = 21.20 \pm 0.40$	$\sigma_5 = 0.55 \pm 0.28$			
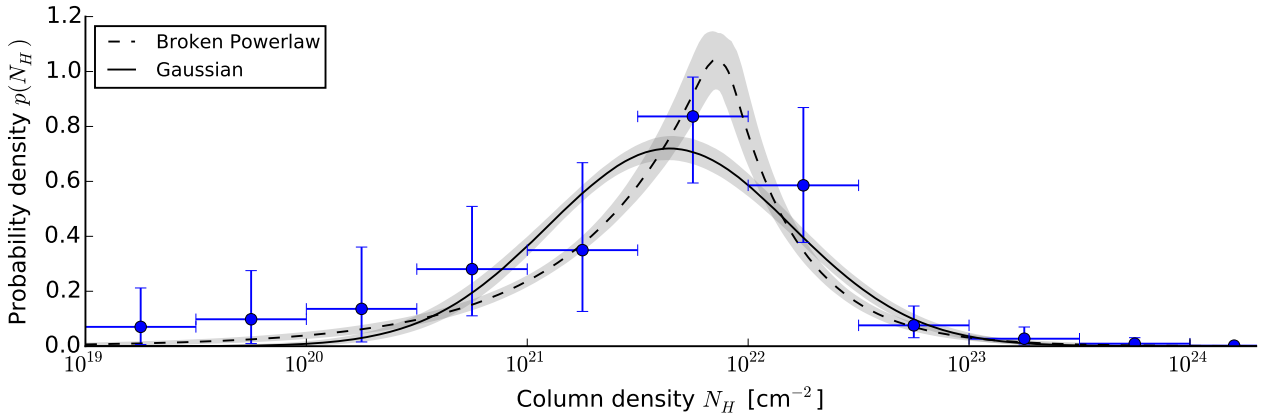
Figure 5. Column density distributions of *Swift*-detected LGRBs. Error bars show 2σ equivalent quantiles.

assumed on μ, $\log \sigma$ and ν, $\log a$, b, and c. In general we find the distribution to be centred at $N_H \approx 10^{21.8} \mathrm{cm}^{-2}$ and effectively spreading two orders of magnitude (see Figure 5). The Gaussian model yields a higher likelihood and since it also has one parameter fewer, is preferred through a lower AIC value. One possibly important difference is that the Gaussian has lighter tails (declining square-exponential) than the broken powerlaw model.

4.2 SingleEllipsoid: A simplistic physically motivated model

While we can model the CDD empirically, we ultimately would like to understand the gas clouds which give rise to the observed column densities. To this end, we present a simple model of a cloud population, which could represent the star-forming region the GRB originated in or the host galaxy. The considered models are gross over-simplifications of the real scenario, which may include multiple absorbers with sub-structure and density gradients sampled in a biased fashion by GRBs. However, as we will show, the simple models are useful to understand the width and shape of the arising distribution.

As an initial toy model, consider a sphere of constant density (radius 1, density 1). For sources distributed uniformly like the gas, the emerging CDD[6] is plotted in Figure 6 (black solid line). The largest possible LOS column density is 2 in these units, corresponding to a full crossing. The most probable column to be observed under random orientations is around 1, with a long tail down to one order of magnitude lower. This scenario is illustrated in the top right corner of Figure 6, with blue crosses indicating the randomly placed sources. Now consider a flatter geometry, an ellipsoid of relative height $z/R = 0.1$ in cylindrical coordinates, illustrated in red in Figure 6. The red curve in the plot shows the corresponding CDD. Here, the distribution is centred at much lower values, around 0.1 (i.e., close to the vertical extent), and it is also very broad, spanning almost three orders of magnitude.

Such a ellipsoid, representing gas that simultaneously obscures GRBs and hosts their progenitors, forms the baseline model of our approach (inspired by, but a generalisation of Reichart & Price 2002, see also Vergani et al. 2004). But this model cannot

---

[6] Numerical details of the computation can be found in Appendix C.
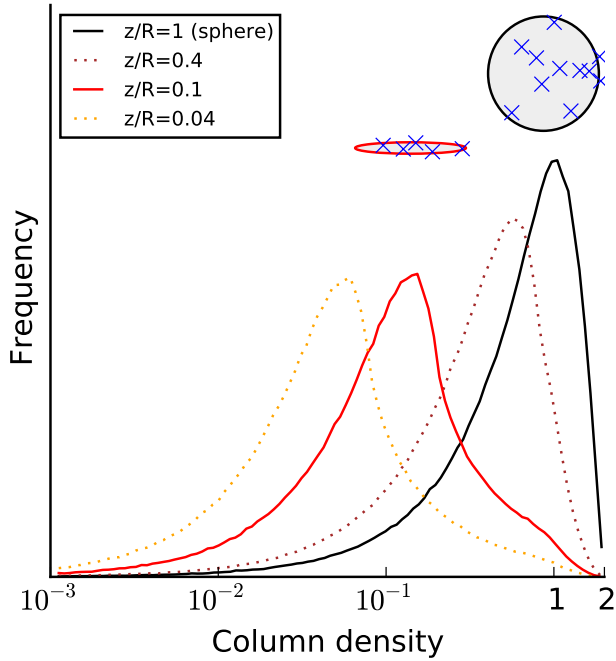
Figure 6. Normalised column density distributions of ellipsoids. A spherical gas distribution, illustrated in the top right corner, is sampled with uniformly distributed sources (blue crosses). The distribution of their column density in random directions is shown by the thick black line in the plot. In other lines we show the cases for cylindrical symmetric ellipsoids with flatter height z to radius R ratios. For instance, the red solid curve shows the case of a $z/R = 0.1$ ellipsoid, also illustrated in red.

Table 5. Parameters of SingleEllipsoid model

Name	Description	Range	Prior
N_H^{major}	N_H along major axis	$10^{20} - 10^{26} cm^{-2}$	log-uniform
σ	scatter of $\log N_H^{major}$	$10^{-3} - 1$	log-uniform
z/R	height/radius ratio	$10^{-3} - 1$	log-uniform

match the data: the derived CDD in Figure 5 is broader and less peaked than those of Figure 6). Actually, it would be very surprising if it did match, because that would imply that all gas clouds in which GRBs reside have the same mass and geometry. We thus define the first physical model to be a population of ellipsoids with the same height/radius ratio, but with a Gaussian distribution of total gas densities. The variance of the population in their column density along the major axis is defined through the parameter $\sigma = \sqrt{var(\log N_H^{major})}$. This is mathematically equivalent to convolving the distributions of Figure 6 with a Gaussian of width σ. Subsequently, this model is referred to as the *SingleEllipsoid* model. The parameters are summarised in Table 5. We constrain them from the redshift subsample in the same fashion as in the previous section.

The parameters exhibit strong degeneracies between the z/R ratio and N_H along the major axis, illustrated in the left panel of Figure 7. The black and red dots indicate the sphere and disk geometries discussed before in Figure 6. However, all the possibilities in this degeneracy yield relatively similar CDDs, shown in Figure 8. The population scatter σ is constrained to 0.22 ± 0.14. This makes the distribution as broad as the empirical model shown in Figure 5. This simple model (SingleEllipsoid) is already a better fit
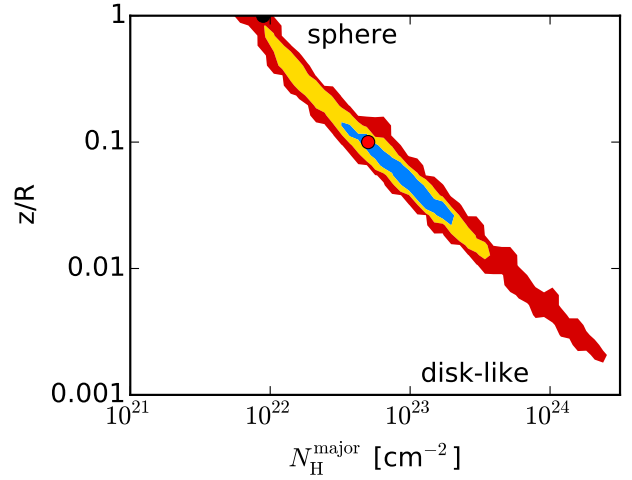
Figure 7. Degeneracy between scale height parameter z/R and the column density along the major axis N_H^{major} in the SingleEllipsoid model. The black and red circle indicate the sphere and disk geometries illustrated in Figure 6. The contours encapsulate 50%, 84% and 99% of the probability.
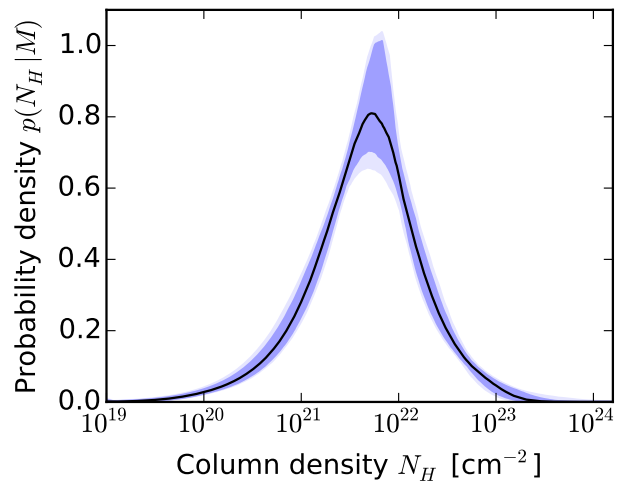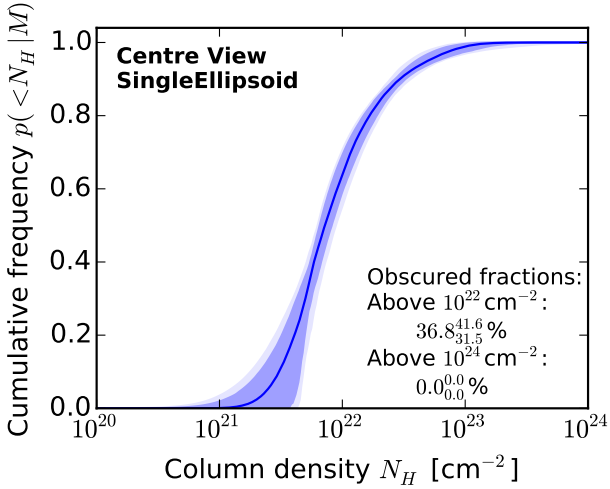

Figure 8. Column density distribution of the SingleEllipsoid model. The dashed line shows the median distribution from the posterior probability distribution. In dark grey shading, the 1σ uncertainty is shown, while light grey shading show the quantiles encapsulating 90% of the probability distribution.

to the data than the empirical Gaussian mixture or Broken Power-law models, and is also preferred by the AIC.

More importantly, however, the SingleEllipsoid model allows us to derive the CDD as it would be seen from the centre of the cloud. This is shown in Figure 9. The central CDD spans the $N_H = 10^{21} - 10^{23} cm^{-2}$ range, with no Compton-thick lines of sight. Under this SingleEllipsoid geometry, up to 50% of the sky would appear obscured with $N_H > 10^{22} cm^{-2}$.

We also investigated possible density gradients by using several co-centred ellipses, each having free shape and density parameters. Such a model can, given enough components, reproduce any monotonically declining density profile. It should also be noted that by embedding a small, dense component arbitrarily large cent-

Figure 9. Cumulative column density distribution of the SingleEllipsoid model as seen from the centre. The solid line shows the median distribution from the posterior probability distribution. In dark shading, the 1σ uncertainty is shown, while light shading represent the quantiles encapsulating 90% of the probability distribution. In this model, about $\sim 40\%$ of the sky as seen from the centre is obscured with $N_H > 10^{22} \mathrm{cm}^{-2}$, while there are no Compton-thick lines of sight.

4.3 Redshift evolution

We investigate evolutionary trends with redshift by adopting independent column density distributions in each of five redshift bins,

$$p(N_H, z | M_{X,z}, \theta) = \begin{cases} p(N_H | M_X, \phi_1) & z < 0.3 \\ p(N_H | M_X, \phi_2) & 0.3 < z < 1 \\ p(N_H | M_X, \phi_3) & 1 < z < 2 \\ p(N_H | M_X, \phi_4) & 2 < z < 4 \\ p(N_H | M_X, \phi_5) & z > 4 \end{cases} \quad . \quad (4)$$

In each redshift bin we adopt the Gaussian or Broken Power-law empirical models. This is chosen despite the above finding that the SingleEllipsoid model is a better fit; the empirical models provide a sufficient characterisation of the CDD and are faster to evaluate. Their parameters are also easier to understand and to compare with other works. The constrained parameter values, using the complete sample, are listed in Table 4 on page 7. The last column lists the AIC model comparison values relative to the single broken powerlaw model (lower is better). The redshift-independent broken powerlaw is preferred over the redshift-dependent variant. For the Gaussian model, the redshift-dependent variant is preferred. This is caused by the significantly lower average column density in the lowest redshift bin $z < 0.3$. Such very local LGRBs are dominated by low-luminosity afterglows which may be a distinct population (Dereli et al. 2015). Uncertainties however remain substantial as few LGRBs exist at low redshifts. At higher redshifts we find no evidence of any redshift evolution, with the CDD always centred at $N_H \approx 10^{21.4-21.8} \mathrm{cm}^{-2}$ with small uncertainties. If any redshift evolution exists there, its effect on the mean column is less than a factor of 3. At very high redshifts ($z > 4$) the evolution
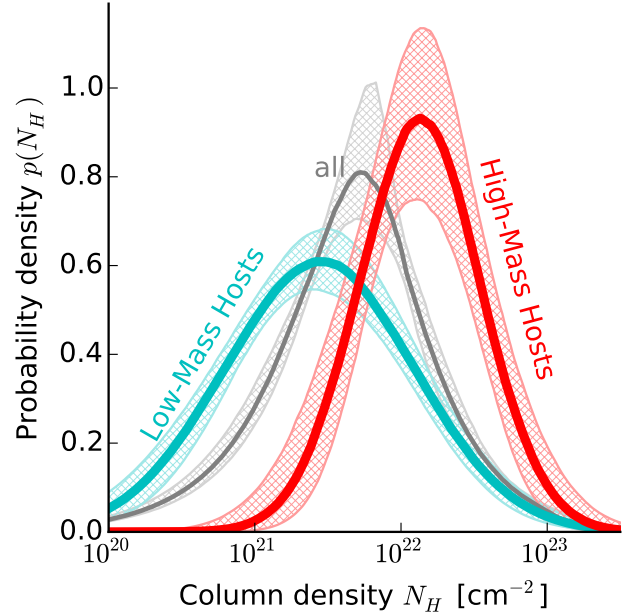
Figure 10. Mass dependence of the column density distribution. LGRBs originating in low-mass host galaxies (cyan, $M_\star < 10^{10} M_\odot$) show lower column densities than those in high-mass galaxies (red, $M_\star > 10^{10} M_\odot$). For the SHOALS sample *Spitzer* observations were used to derive stellar masses (Perley et al. 2016c). In grey, the SingleEllipse model for all LGRBs is shown.

Table 6. Gaussian model parameters for different samples.

Parameter	Mean log N_H	Std. deviation σ
Complete sample	21.64 ± 0.03	0.55 ± 0.03
Low-mass sub-sample	21.44 ± 0.09	0.65 ± 0.07
High-mass sub-sample	22.13 ± 0.10	0.43 ± 0.09
Redshift sub-sample	21.49 ± 0.06	0.58 ± 0.05

is again uncertain because the imprint of absorption is redshifted below the X-ray regime. The uncertainties in Table 4 indeed highlight that the strongest constraints come from the $z = 0.3 - 4$ redshift range. If we replace the model in that range with a SingleEllipsoid model, the uncertainties of Figure 7 shrink and the spherical obscurer is ruled out with 99% probability. We also note that the redshift-independent models are always preferred, i.e., no significant redshift evolution is found, when adopting the SHOALS sample.

4.4 Host mass dependence of the N_H distribution

Perley et al. (2016c) investigated the galaxy mass of LGRB hosts and found that above $M_\star = 10^{10} M_\odot$ virtually all of their LGRBs had dusty/obscured afterglows. Their SHOALS sample was constructed only using observability criteria, i.e., quantities that are unrelated to the host galaxy mass and LGRB obscuration (see Perley et al. 2016b, for details). This subsample selection was then targeted with very deep follow-up observations to derive redshifts and host galaxy masses. We adopt their highly redshift-complete sample and split it at $M_\star = 10^{10} M_\odot$ into a low-mass and high-mass subsample (data are described in more detail in Section 3). We analysed each subsample with the Gaussian model. We find that the column densities are drastically different between the low-mass and

high-mass samples, as illustrated in Figure 10: The high-mass sub-sample shows a five times higher mean column density. In other words, high-mass host galaxies are preferentially associated with obscured LGRBs, while a sizeable fraction of low-mass host galaxies have unobscured LGRBs. The corresponding parameter values are listed in Table 6.

4.5 A mass - column density relationship

We have now established that the primary driver of the diversity of LGRB column densities is host galaxy mass, not evolution with redshift. Consequently we fit a model for the distribution that is stellar mass dependent. We convert the *Spitzer* $3.4\mu m$ magnitudes given in Perley et al. (2016c) to masses according to their model. Adopting instead the relation of Meidt et al. 2014 does not change our results significantly.

Figure 11 shows our data in stellar mass - $N_{\rm H}$ space. A clear increase in the column density with mass can be observed, with no LGRBs in host galaxies of $M_\star < 10^9 M_\odot$ exhibiting $N_{\rm H} > 10^{22} {\rm cm}^{-2}$, while such sources exist for more massive hosts. However, there is substantial scatter in the diagram. We first fit a power-law model including a systematic Gaussian scatter for $\log N_{\rm H}$. Our fitting method is as before and takes into account the upper limits, but the CDD model is now mass-dependent. Our relationship can be written as:

$$\log N_{\rm H} = 21.7 + 0.38 \cdot (\log M_\star/M_\odot - 9.5) \qquad (5)$$

Figure 11 plots the relation (red dashed line) with its data uncertainties (grey shading). The data uncertainties are for the intercept $\overline{N_{\rm H}} = 21.67 \pm 0.06$ and the slope 0.38 ± 0.06. The determined exponent of approximately $\frac{1}{3}$ is noteworthy. The powerlaw relation of equation 5 connects the line integral $N_{\rm H}$ on the left with the volume integral $M_\star$ on the right hand side. If both simply scale geometrically with galaxy size ($N_{\rm H} \sim r$, $M_\star \sim r^3$), and the obscuration is primarily due to the host galaxy, a exponent of $\frac{1}{3}$ is expected.

We have simultaneously constrained the remaining intrinsic scatter as a normal distribution. Its standard deviation is $\sigma = 0.49 \pm 0.05$ around the relation, shown as a blue error bar on the right of Figure 11. If instead of a normal distribution we adopt the SingleEllipse model, the scatter is consistent with zero. In other words, the observed scatter can be fully explained by the mass distribution and geometric effects.

4.6 Redshift incompleteness bias

Many previous works have only considered LGRBs with determined redshifts, which is liable to introduce a bias against faint, dust-extincted hosts. To investigate the nature of this redshift incompleteness bias, we analyse the redshift subsample, i.e., limit ourselves to LGRBs with determined redshifts in the $z = 0.3 - 3.2$ range. The derived Gaussian model parameters are listed in Table 6. Compared with the complete sample, the $N_{\rm H}$ distribution is centred at lower column densities. This indicates a bias against obscured LGRBs. In fact, the derived parameter values are most similar to the low-mass subsample, with the break and low-$N_{\rm H}$ slope having the exact same values, and the high-$N_{\rm H}$ slope falling within 1σ of the uncertainty. This finding reproduces early works which used only LGRBs with determined redshifts and found that these only occur in low-mass host galaxies: The bias on the $\log N_{\rm H}$ distribution appears as if only low-mass host galaxies had been selected.
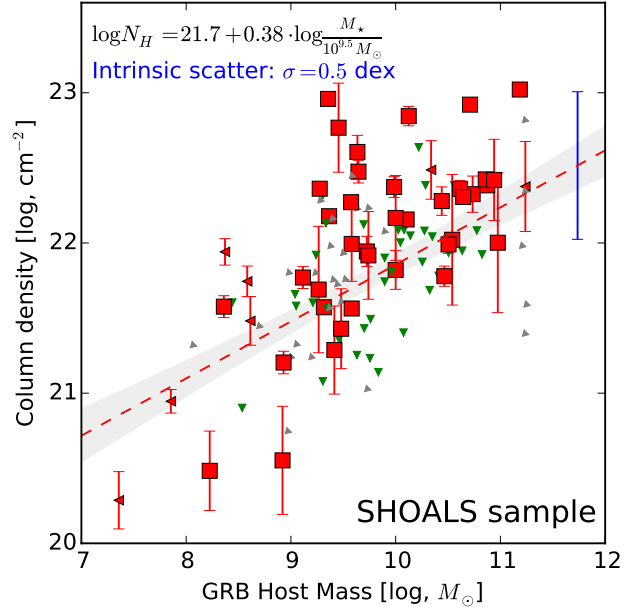
Figure 11. Host mass - column density relation. Points are individual GRBs in the SHOALS survey. Red squares indicate constraints in mass and column density, green downward pointing triangles are upper limits in column density, grey triangles indicate upper limits in both. Columns thicker than $N_{\rm H} = 10^{22} {\rm cm}^{-2}$ are only observed for galaxies more massive than a billion suns. A powerlaw fit is shown as a red dashed line. Grey indicates the uncertainty around the slope, while the blue error bar indicates the systematic scattering around the powerlaw for individual objects.

5 DISCUSSION

5.1 The column densities of the GRB population

We have analysed the column density distribution of GRBs as probes of the gas distribution in their host galaxies. We used state-of-the-art statistical methods to propagate uncertainties in the spectral analysis and redshift into the population analysis, while remaining careful of biases from incomplete redshift information.

In the complete sample, most of the 512 GRBs have column densities below $10^{21.5} {\rm cm}^{-2}$, with the most extreme spectrum showing $10^{23} {\rm cm}^{-2}$ (see Figure 4). The population can be empirically fitted using a broken powerlaw distribution which shows a steep decline towards high obscurations (slope of ~ -1.2) and a long tail towards low obscurations (slope of 0.75), spanning the $10^{20-23} {\rm cm}^{-2}$ range. Thus, heavily obscured (e.g. Compton-thick) LGRBs, if they exist at all, must be extremely rare. They have not been seen although XRT is sensitive enough to detect[7] and characterise them (see Section 4). Using model selection we concluded that a better empirical description is provided by a normal distribution centred at $\log N_{\rm H} = 21.6$ with intrinsic scatter of $\sigma = 0.6$.

In a series of papers, Campana and collaborators investigated the column density distribution of LGRBs as a population. Campana et al. (2010a) updated the results of Campana et al. (2006)

---

[7] In principle, a second class of GRBs could exist behind even more extreme columns (e.g., $N_{\rm H} \gtrsim 10^{25} {\rm cm}^{-2}$) so as to render the GRBs undetectable even in the BAT energy band. This would require a conspicuously bimodal column density distribution which we do not consider probable a-priori. Such a high column density would almost certainly have to be local to the GRB.
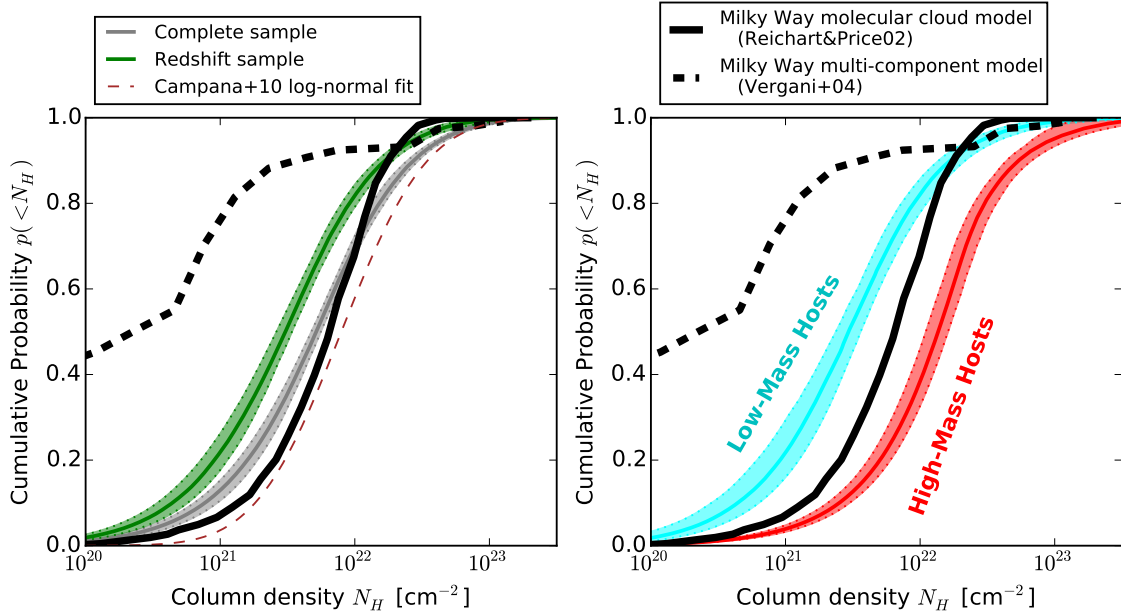
Figure 12. Comparison to literature results. Thick solid lines show the models of Reichart & Price (2002) and Vergani et al. (2004) where GRBs are placed randomly in gas components of the Milky Way; Reichart & Price (2002) is restricted to molecular clouds. The cumulative column density distribution from the four samples used in this work is plotted when adopting the *Gaussian* model (solid: median, shading: 1σ quantiles). *Right panel*: Selection of low-mass (*cyan*) and high-mass (*red*) subsamples show the importance of the host galaxy. *Left panel*: The complete sample distribution (*grey*) is very close to the Vergani et al. (2004) model. The (biased) redshift subsample (*green*) lies systematically at lower columns by about 0.3dex, similar to the low-mass subsample in the right panel.

and analysed a sample of 93 *Swift*-detected LGRBs with redshift measurements. They performed a broken powerlaw fit and find the break of the distribution at $a = 21.71^{+0.14}_{-0.15}$, with slopes $b = 1.59^{+1.81}_{-0.57}$ and $c = -0.78^{+0.42}_{-0.26}$. This is approximately the same peak as found in this work, but they find a steeper decline towards low-N_{H} (b) and a shallower decline towards high-N_{H} (c) in the population. This difference is probably due to the handling of the uncertainties in X-ray spectra and the population analysis. Many sources in their as well as our analysis show large uncertainties in N_{H} as derived from spectral analysis. Errors such as in $2.4^{+1.7}_{-1.5} \times 10^{21} \mathrm{cm}^{-2}$ are common, and essentially include the possibility of negligible intrinsic obscuration. Notably the lower error estimate often includes values one or two orders of magnitude lower, while the upper error only doubles the value. In log-space, the best-fit N_{H} estimator is thus biased towards the upper limit. This work adopts a Bayesian methodology to propagate the uncertainties into the population analysis, which also allows us to treat upper limits consistently.

The obscuration of LGRBs depends strongly on their host galaxies. LGRBs in high-mass galaxies show higher absorbing columns by ~ 0.7 dex versus those originating in low-mass galaxies, as shown in Figure 10. This agrees with the findings at optical wavelengths of Perley et al. (2016c), where massive host galaxies are virtually always associated with absorbed/dusty afterglows. This suggests that the obscurer may be primarily the host galaxy itself, with high-mass galaxies being capable of attracting and holding larger quantities of gas (see more discussion in the next section). Importantly, this biases the results when incomplete samples are used: Campana et al. (2012) noted the bias of Campana et al. (2010a), which appears when considering only LGRBs where the redshift is determined, as dust-extincted afterglows are fainter and often are harder to obtain spectra of. They use a unbiased sample of 58 bright LGRBs and find similar results to Campana et al. (2010a),

when comparing a Gaussian fit. This work adopted the SHOALS sample, which is similar in spirit but larger in size (112 objects, Perley et al. 2016b). Using newer spectral models which incorporate effects relevant at high obscuring columns and improved spectral analysis methodology we are able to make stronger inferences in the derived column density distribution (Table 4). We find that the bias of considering only LGRBs with determined redshifts is severe, and that it approximates the exclusion of all massive host galaxies (see Table 6). The aforementioned effects can be seen in the left panel of Figure 12, where we compare the redshift sample to the complete sample.

Campana et al. (2010a) and Campana et al. (2012) also investigated a possible redshift evolution of the obscuration. This is interesting because star forming regions at high redshift, particularly at the peak of star formation at $z = 1 - 3$, may be more compact. They claimed that high-redshift GRBs ($z > 4$) are more obscured than low-redshift GRBs. This is based on a KS-test which yields a p-value of 0.08 that the best-fit column densities are drawn from the same distribution. P-values are uniform random variates, such that the frequency of yielding such a result or a more extreme one is high (10%, but increasing with the number of tests performed), indicating a substantial probability of a false positive. Campana et al. (2012) makes more cautious claims due to the smaller sample size of their unbiased sample. Even if significant, the best-fit N_{H} values cannot be drawn from the same distribution in principle, because the spectral window probed is different. Furthermore, splitting the sample is problematic because a high percentage of GRBs have uncertain redshifts. To overcome the limitations of the KS test, in this work we simultaneously fitted independent distributions in 5 redshift intervals ($z < 0.3$, $z = 0.3 - 1$, $1 - 2$, $2 - 4$, $z > 4$) and compared their parameters. We find consistent parameters (see Table 4) in the relevant redshift bins, indicating no redshift evolution around the

peak of star formation. If any redshift evolution of the obscurer is present, it is limited to modifying the obscuring columns by a factor of 3, and thus less important than the host galaxy mass. An exception is the $z < 0.3$ redshift bin, which shows lower obscuration on average. This may be explained by a dominant low-luminosity GRB population in that redshift range, which form a distinct population (Dereli et al. 2015). Alternatively, it could be a side-effect of galaxy-mass downsizing, which is more pronounced in GRBs (Schulze et al. 2015; Perley et al. 2016c) than in the general galaxy population (e.g. Fontanot et al. 2009).

5.2 LGRB obscurer models

Reichart & Price (2002, RP02 hereafter) developed a obscurer model based on the distribution of molecular clouds in the Milky Way. Their mean radial column densities are $N_H^{major} \approx 10^{22} cm^{-2}$ with a scatter of 0.2 dex in their population. Such a cloud distribution, when including random placement and orientation in such clouds, was found to be consistent with observations in the analysis of RP02 with 15 GRBs, and also in the analysis of Campana et al. (2006) and Campana et al. (2010a) which included *Swift* observations. Vergani et al. (2004) developed a multi-component gas model of the Milky Way and simulated the LGRB column density distribution with ray-tracing. They however assumed that a large portion of LGRBs may occur in diffuse gas. This includes the disk, leading to a high percentage of LGRBs with low column densities. Campana et al. (2006) ruled out that model based on their derived column density distribution, and concluded that LGRBs likely originate in molecular clouds (the remaining model). A limitation of the RP02 molecular cloud model is that it is based on the Milky Way, which is atypical in mass and metallicity for LGRB host galaxies. In this work we developed a more general approach by deriving the properties of the LGRB obscurer population from the data.

We find that the column density distribution of LGRBs can be well-described by a simple model: a single gas component of uniform density, in which LGRBs are randomly located. The geometry and major axis column density of the cloud population were tentatively constrained (see Figure 7) to a flat disk with a height-to-radius ratio of 1 : 20 and a major axis column density of $N_H^{major} \approx 10^{23} cm^{-2}$. To explain the broadness of the column density distribution, the best-fit model has a scatter in $\log N_H^{major}$ of $\sigma \approx 0.22 \pm 0.14$ (the 10% quantile is at 0.03). For comparison, the RP02 model used an essentially flat distribution of scatter $\sigma = 0.2$ dex between molecular clouds in the Milky Way. The clouds in the RP02 model have a density gradient, are spherical and therefore match the data with a lower maximal column density. The right panel of Figure 12 shows the RP02 Milky Way model in comparison to our results using the high-mass and low-mass subsamples, which probe stellar masses comparable to, and below that of the Milky Way. The RP02 model falls in between the constraints from those samples, implying that LGRBs in Milky Way-size galaxies are more obscured than what the RP02 Milky Way model predicts. Figure 12 also compares the multi-component model of the Milky Way gas components by Vergani et al. (2004). That model assumes that GRBs can also originate in the atomic hydrogen of the thin disk, which leads to many GRBs with low column densities. This model is clearly ruled out, leaving the origin of GRBs in galactic molecular clouds as a plausible scenario. In that case however the column density of the molecular clouds would have to increase with galaxy host mass, which is not the case in nearby galaxies (Larson 1981; Bolatto et al. 2008; Lombardi et al. 2010). The geometry constraints suggest another
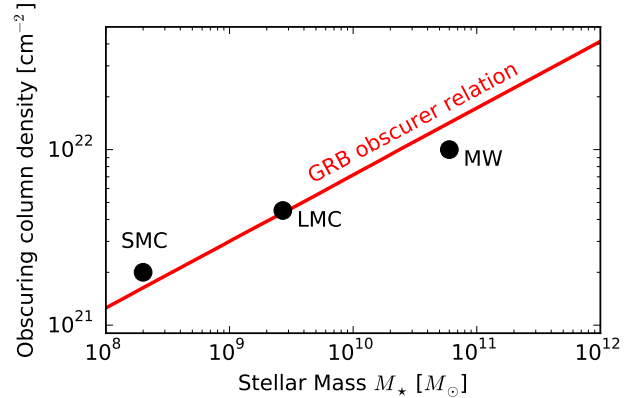

Figure 13. Column densities of local galaxies. We derived the densest column densities seen in the LMC and SMC, by taking the 99% highest values from HI radio maps and correcting for metal abundances to derive a N_H as would be seen by X-ray observations. For the Milky Way (MW) we use the map of Dickey & Lockman (1990). The obscuration of galaxy gas of each of these local galaxies falls exactly on the relationship we derive from GRB obscuring column densities (black line).

possibility however: giant molecular clouds could be arranged in a relatively flat disk in which the GRBs are produced. The number of clouds (and thus the major axis density) should then scale with the size of the galaxy, as more massive galaxies can hold larger quantities of gas. This scenario of the galaxy acting as the primary obscurer appears more likely due to the $N_H^3 \propto M_\star$ relation found (Equation 5 in Section 4.5).

5.3 Local Galaxies as Obscurers

We verify the mass dependence of the obscurer by determining how well local galaxies act as obscurers. The Milky Way, the Large Magellanic Cloud (LMC) and the Small Magellanic Cloud (SMC) cover a large stellar mass range and their column density of N_H is well mapped. Our relationship depicted in Figure 11 predicts that at Milky Way stellar masses, $M_\star = 6 \times 10^{10} M_\odot$ (McMillan 2011), the average galaxy should have some LOS column densities above $N_H > 10^{22} cm^{-2}$. Galactic column density maps of the Milky Way, as depicted in Figure 1, show that a small fraction of the sky ($\sim 1\%$) is indeed obscured with $N_H > 10^{22} cm^{-2}$ as seen from our vantage point. The fraction may be larger from more central regions of the Galaxy, or from the vicinity of blue, star forming regions where LGRBs are typically found (Bloom et al. 2002; Fruchter et al. 2006). The Milky Way however lies at the massive extreme when compared with the host galaxies of LGRBs. The LMC is perhaps a more appropriate galaxy to consider, with a stellar mass of $M_\star \sim 3 \times 10^9 M_\odot$. Its observed LOS column density reaches values up to $N_H \approx 3 \cdot 10^{21} cm^{-2}$, with the star-forming region 30 Dor reaching $N_H \approx 9 \times 10^{21}$ (Brüns et al. 2005). Using the ellipticity ($\epsilon \approx 0.3$) and inclination ($i \approx 30°$) of the LMC (see van der Marel 2006, for a review of various measurements) the major axis column density should be lower than the observed column density by a factor of 60%. Therefore, from the centre of the LMC the entire sky has LOS column densities below $N_H < 10^{22} cm^{-2}$. That is again consistent with our $N_H^3 \propto M_\star$ relationship, which predicts that such sight lines should be very rare for LMC-mass galaxies. Finally we consider the SMC, with a stellar mass $M_\star \sim 3 \times 10^8 M_\odot$ (van der Marel et al. 2009). While that galaxy has a smaller HI mass, its
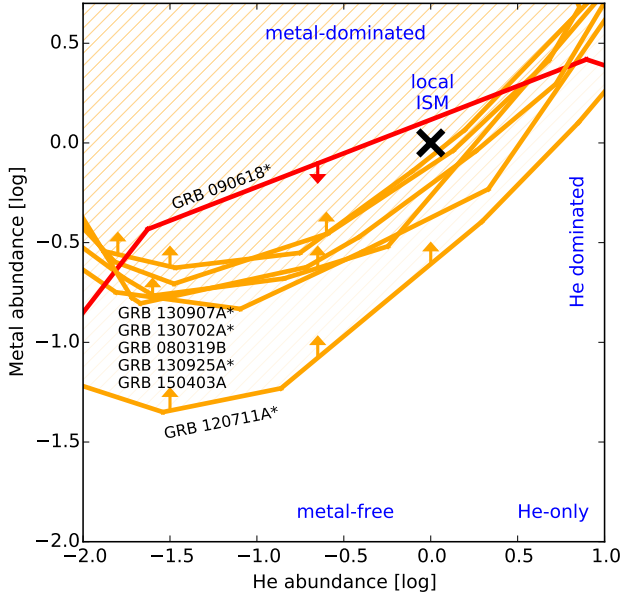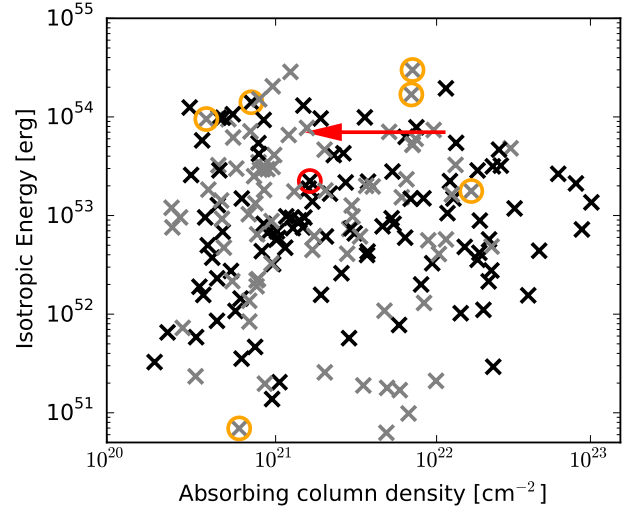
Figure 14. LOS metal abundances for seven LGRBs where the He and metal abundances could be constrained. The 3-sigma contours (orange thick lines) of six spectra exclude metal-poor and He-abundant solutions. For GRB 090618 (red thick line), metal-rich abundances are excluded. All shown LOS's are consistent with the abundances of the local ISM (cross, Wilms et al. 2000). A metal-free, Helium-dominated absorber can be rejected at high significance. LGRBs marked with asterisks show super-galactic N_H/A_V ratios.


Figure 15. The relation between obscurer and LGRB energy. We plot the effective column density (neutral absorber with local ISM abundances) against the isotropic energy for sources where the redshift is known. Black crosses are from the SHOALS sample, grey crosses denote other LGRBs where the X-ray afterglow spectrum exceeds 1000 counts. The circles indicate the same objects shown in Figure 14, where there is evidence of metals in the X-ray absorption. The red arrow indicates a reduction in the effective column density by a factor of seven if dense circum-burst material were ionised by highly energetic bursts. However, no such systematic shift is apparent when comparing to lower energy bursts.

N_{HI} is higher than in the LMC, reaching $N_H = 10^{22} \mathrm{cm}^{-2}$ (Brüns et al. 2005). One should keep in mind that for the SMC and LMC we relied on HI columns derived from radio observations, whereas everywhere else in this paper we consistently use X-ray determined metal columns converted into N_H assuming solar abundances. Therefore the N_H values we should compare with for the SMC and LMC – their metal columns – actually should be lower given their low gas metallicity of 0.2 and 0.5 solar, respectively (Tchernyshyov et al. 2015). Taking the metal abundance into account, we contrast these three local galaxies (MW, LMC and SMC) in Figure 13 against our relationship and find excellent agreement.

5.4 A Helium-dominated, circum-burst absorber?

An open issue in the understanding of LGRB afterglow is the inconsistency between optically and X-ray-derived absorption. The rest-frame UV extinction, A_V, and the X-ray derived column density, N_H, show a tendency toward lower-than-galactic ratios and broad scatter (e.g. Schady et al. 2011; Watson et al. 2013). This can be caused by deviations in abundances, dust-to-gas ratios and/or ionisation states compared to the galactic ISM. To resolve this inconsistency goes beyond the scope of this work. However, we study one recently proposed explanation in detail. Watson et al. (2013, W13 hereafter) postulated that gas in the vicinity (< 30pc) of the burst provides the bulk of the X-ray absorption. The powerful burst emission can destroy dust, fully ionise all hydrogen atoms (which have a low ionisation energy) and O and Fe atoms (which are few in number) along the LOS. These atoms would therefore not absorb X-rays. However, for certain luminosities, not all He atoms would become ionised, because of their large number. W13 showed that a He-dominated X-ray absorption spectrum is observationally indis-

tinguishable from one with local ISM abundances in typical X-ray spectra.

In a few cases where photon statistics are robust, the effective abundance of metals and helium can be constrained directly. We set the helium and metal abundances each as free parameters in our fit (TBVARABS model, Wilms et al. 2000), and analysed all LGRB XRT spectra with more than 5000 counts (42 sources). The normalisation, photon index and column density were also free parameters. In seven cases, shown in Figure 14, the abundances could be constrained. These have more than 30000 photon counts each. We comment on some individual sources in Figure 14 in detail: We note that Giuliani & Mereghetti (2014) found a metal-free solution ($Z/Z_\odot < 0.05$) when analysing a *XMM-Newton* spectrum of GRB 120711A. The difference may be because we use a slightly higher galactic column density of $1.06 \times 10^{21} \mathrm{cm}^{-2}$ following Evans et al. (2009) and more recent absorption model and cross-sections in our fit. Our abundance contours for GRB 090618 are consistent with those from the *XMM-Newton* spectral analysis of Campana et al. (2011). They could also place a lower limit of $Z/Z_\odot > 0.2$. For GRB 130925A and GRB 130907A we additionally excluded the (early-time) WT mode spectra that may still be, despite our efforts of Section 3.2, slightly contaminated by prompt emission. Nevertheless we obtain constraints with the (late-time) PC mode data alone. For GRB 130925A, we note that Schady et al. (2015) derived super-solar metallicity from optical spectroscopy. Particular noteworthy is GRB 130702A. This LGRB is associated with a supernova hosted by a dwarf galaxy with $M_\star \approx 10^8 M_\odot$ (Kelly et al. 2013), and hence represents a typical LGRB. In all cases, the constraints exclude a He-dominant absorber but are consistent with the abundances of the local ISM.

Additionally, if the LGRB is responsible for ionising substantial fractions of the absorber, the effective absorbing column
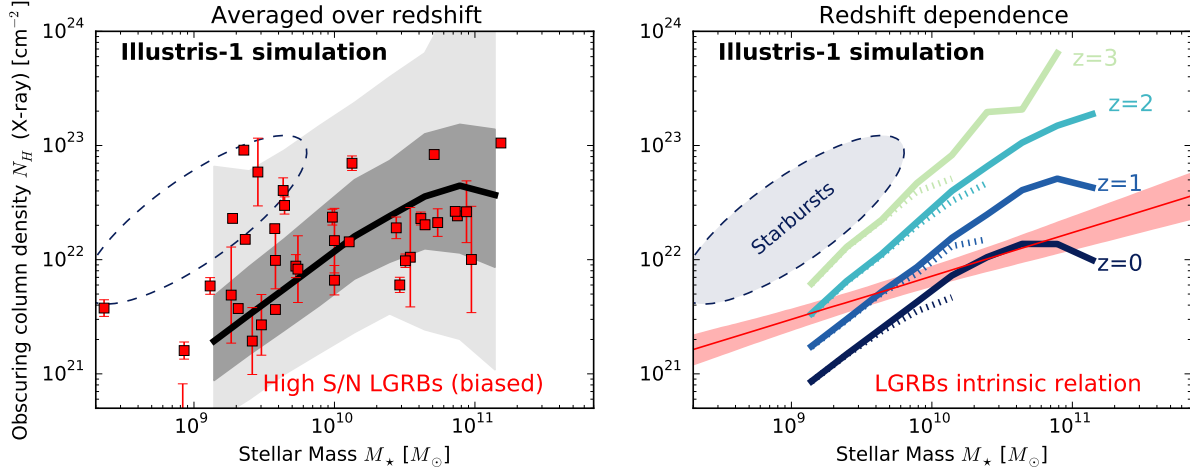
Figure 16. Obscuration in simulated galaxies. *Left panel*: The grey shaded regions show the 1 and 3 sigma range of the distributions in median N_H as seen from the densest region. The black line marks the median. Individual observed LGRBs are overlaid as red error bars (same as in Figure 11). While in the left panel redshift snapshots have been combined according to the SHOALS redshift distribution, the *right panel* shows the median as a function of redshift (thick lines). Dotted lines indicate the effect of only using simulated galaxies with sub-solar stellar metallicity. In red, our $N_H - M_\star$ relation is shown. The ellipse indicates (for $z = 0$) a sub-population in the simulation showing elevated obscuring columns. These are predominantly star-burst galaxies.

should be reduced for more energetic bursts. Campana et al. (2012) find no significant difference in the column distribution of bright bursts. In Figure 15 we show the distribution of sources in isotropic energy and effective column density N_H for sources with redshift information. The isotropic energies were computed using the method of Bloom et al. (2003)[8]. Effective column densities were derived using a local ISM abundance, neutral absorber model. The SPHERE model is used, which is valid also for the highest absorbing columns, as discussed in Section 3.3. There does not appear to be a burst energy-dependence in the absorber properties. If the burst energy ionised metals and hydrogen, reducing the effective column density by a factor of seven (example calculation in W13, red arrow), we would expect a deficit of sources in the upper right quadrant of the plot. However, no deficit of high-obscuration sources at the luminous end is apparent in Figure 15, and the column density distribution appears independent of energy. In Figure 15, only GRBs for which redshifts have been determined are shown, which reduces the number of faint, obscured bursts (lower right quadrant). To avoid such biases, black crosses show LGRB from the SHOALS survey. Additionally, metals have been detected in highly-absorbed, energetic bursts: Orange circles in Figure 15 show the same sources as in Figure 14.

The correlation of column density and stellar mass dependence is a strong argument that the X-ray column density is *predominately* due to the host galaxy-scale gas. The lack of energy-dependence of the absorber support the dominance of a distant obscurer. Abundance measurements suggest that the X-ray obscurer can be modelled similar to the local ISM. Under local ISM abundances, the dominant absorbers are Fe and O. Partial ionisation of metals may still be present and account for deviations in A_V, but its effect on the X-ray spectrum appears negligible. Furthermore, relatively low galaxy-scale column densities can occur if the LOS does not pass through the galaxy (left tail in Figure 6, particularly objects below the $M_\star - N_H$ relation in Figure 11). In these cases,

the dominant obscurer could be the local environment, where hard burst radiation destroying dust may reduce the A_V/N_H ratio. However, fully resolving the discrepancy between N_H and A_V measurements is beyond the scope of this work.

5.5 Obscuration in simulated galaxies

At higher redshifts the gas content of galaxies is not easily accessibly through observations. Instead we turn to simulated galaxies from hydrodynamic cosmological simulations. This exercise is potentially predictive because the amount of gas inside galaxies is constrained by the simulation's requirement to start with the Big Bang's density and to reproduce today's stellar mass function. In galaxy evolution models, the massive end of the existing stellar population expels metals into the galaxy. The metal gas produced per stellar mass is determined by the chosen IMF and the metal yield, with the latter tuned to reproduce the stellar mass function (Lu et al. 2015). The total metal gas mass residing in galaxies further depends on the chosen feedback models, which can expel gas out of the galaxy. Typically the metal gas mass inside galaxies follows a $M_Z/M_\star = 1 : 30 - 1 : 100$ relation in semi-analytic models at $z = 0 - 3$ (e.g. Croton et al. 2006, 2016). The crucial remaining question surrounds the arrangement of that gas inside galaxies, as the concentration of gas defines its column density – this requires hydrodynamic simulations.

The *Illustris* simulation (Vogelsberger et al. 2014b,a) is a cosmological hydrodynamic simulation which attempts to reproduce the galaxy population using state-of-the-art star formation, supernovae and AGN feedback mechanisms inside dark matter haloes. *Illustris* reproduces many observed quantities; most relevant for this work it reproduces roughly the stellar mass distribution of galaxies, their morphology, and gas content from CO observations (Vogelsberger et al. 2014b; Genel et al. 2014). The gas particle resolution in *Illustris* is adaptive, with some cells being as small as 48pc in the highest resolution simulation (*Illustris-1*) used here, indicating that today's cosmological simulations indeed resolve galaxies into small substructures.

We apply ray-tracing, treating each simulated galaxy

---

[8] In a few cases where the peak energy could not be constrained, the values were taken from Butler et al. (2010).

(subhalo) separately. The starting point is the densest region, presumably representing a region of star formation. From that position, we radiate along random sight-lines all metal gas bound to the subhalo. In *Illustris*, gas is represented by Voronoi cells, therefore we Voronoi-tessellate the ray and assign each part the corresponding cells density and finally sum to a total metal column density. We then compute a equivalent hydrogen column density distribution by converting under Wilms et al. (2000) solar abundances to N_H. This mimics how N_H is derived in X-ray observations. We adopt $h = 0.7$ and work in physical units at redshift slices $z = 0, 1, 2$ and 3. We investigate all galaxy subhaloes with $M_\star > 10^9 M_\odot$ (as smaller galaxies are difficult to resolve).

The first question to address is whether the gas in simulated galaxies reproduces the same N_H values as observed. The left panel of Figure 16 shows several individual LGRBs from the SHOALS sample, specifically those with host mass and N_H measurements. Overlaid are the results of the simulation snapshots, redshift-weighted according to the SHOALS redshift distribution. Grey shading represents the distribution of the median N_H of individual simulated galaxies. We find that the observations overlap well with the simulations under the assumption that LGRBs originate in dense regions of galaxies. We also find that the simulations predict a diversity of galaxies with a scatter of ~ 0.5 dex in N_H, in agreement with our observations. We test the importance of the immediate vicinity to the N_H by excluding the inner 100 pc radius, which reduces N_H by a factor of 2 on average. This indicates that distant, i.e., galaxy-scale obscuration is important.

In both the observations and simulations, some rare objects occupy the upper left quadrant of Figure 16, showing high obscurations $N_H > 10^{22}$cm^{-2} despite low masses $M_\star < 10^{10} M_\odot$. In the simulations, these galaxies have high star formation rates, with the majority being starburst galaxies and many having recently experienced mergers. Figure 16 indicates the relevant range with an ellipse for $z = 0$ (other redshifts are slightly higher).

The right panel of Figure 16 depicts the redshift evolution of simulated galaxies. In *Illustris*, $z = 1 - 3$ galaxies have a slightly higher specific gas content, which affects the median column densities. At low redshifts ($z = 0 - 1$), massive galaxies in particular loose gas by strong feedback from active galactic nuclei to avoid over-production of massive galaxies. From our observations we ruled out a redshift-dependent trend of LGRBs in Section 4.4[9]. Furthermore, at each redshift the slope of the $N_H - M_\star$ relation derived from *Illustris* is substantially steeper than $\frac{1}{3}$.

These two issues indicate that the *Illustris* simulation may not represent the gas in galaxies correctly, because it predicts substantially more obscured LGRBs and higher columns for LGRBs in massive galaxies. If remaining concerns e.g., regarding absorber geometry and substructure can be addressed, our X-ray tomography of galaxy gas could be used in the future to distinguish (the strength of) feedback models and star formation efficiencies (see also Paper II). Alternatively, the lower observed obscuration may be due to a environmental preferences of LGRBs inside galaxies, such as a metal/dust aversion.

---

[9] The same result occurs when adding a redshift-dependence to the $N_H - M_\star$ relation; the individual constrained SHOALS LGRBs also do not appear to follow that redshift evolution.

6 SUMMARY

We analysed a large sample of *Swift*-detected long-duration Gamma-Ray Bursts using modern statistical techniques, incorporating the uncertainties from spectral analysis and investigating the effect of redshift incompleteness from dust-extinct/dark LGRBs. Our findings can be summarised as follows:

(i) The column density of the LGRB population lies in the 10^{20-23}cm^{-2} range and can be described by a normal distribution.

(ii) A well-suited model for the column density distribution is a axisymmetric ellipsoid of gas with randomly placed GRBs within. This set-up generalises previous models based on the giant molecular clouds of the Milky Way. Those in fact have lower column densities than observed from GRBs in host galaxies of similar mass. Permitted solutions for the obscuring clouds include a degenerate range of densities and flatness ($\sim$1:20). Additionally it is necessary that the gas ellipsoid population has a distribution in its total gas density of about 0.22 dex.

(iii) We systematically search the *Swift* archive for evidence of heavily-obscured LGRBs. We note that such LGRB could have been detected and characterised by *Swift*/XRT given their intrinsic X-ray luminosities, but are not observed. LGRBs therefore do not reach heavily obscured column densities of $N_H > 10^{23}$cm^{-2}.

(iv) The column density of LGRBs shows no significant evolution with redshift. If present its effect is at most a factor of 3.

(v) LGRBs in galaxies of high stellar mass show substantially more obscuration. We find a novel relation:

$$N_H = 10^{21.7}\text{cm}^{-2} \times \left(M_\star/10^{9.5} M_\odot\right)^{1/3}$$

(vi) The scatter in column densities can be fully explained by the mass-dependence (v) and geometric effects (ii).

(vii) We argue based on the mass-dependence of the obscuration and the derived geometry of the obscurer as well as analysis of well-mapped local galaxies, that **the obscurer is predominantly the GRB host galaxy itself**.

(viii) This conclusion is corroborated by investigating the metal gas mass in simulated galaxies. These predict the same magnitude of obscuring X-ray column densities, similar scatter as well as a mass-dependence, although of a steeper slope.

tion package CIAO and Sherpa. Additionally, the BXA[10], PyMultiNest[11], Astropy (Astropy Collaboration et al. 2013) and CosmoloPy[12] software packages were used.

References

Aird J., et al., 2010, MNRAS, 401, 2531
Aird J., Coil A. L., Georgakakis A., Nandra K., Barro G., Perez-Gonzalez P. G., 2015, preprint, (arXiv:1503.01120)
Akaike H., 1974, Automatic Control, IEEE Transactions on, 19, 716
Anders E., Ebihara M., 1982, Geochimica Cosmochimica Acta, 46, 2363
Antonelli L. A., et al., 2010, GRB Coordinates Network, 10620
Aoki K., Hattori T., Kawabata K. S., Kawai N., 2006, GRB Coordinates Network, 4703
Astropy Collaboration et al., 2013, A&A, 558, A33
Barthelmy S. D., et al., 2009, GRB Coordinates Network, 9756
Barthelmy S. D., et al., 2012, GRB Coordinates Network, 13910
Berger E., Gladders M., 2006, GRB Coordinates Network, 5170
Berger E., Rauch M., 2008, GRB Coordinates Network, 7389
Berger E., Soderberg A. M., 2005, GRB Coordinates Network, 4384
Berger E., Gladders M., Oemler G., 2005a, GRB Coordinates Network, 3201
Berger E., Geha M., Thompson I., 2005b, GRB Coordinates Network, 3753
Berger E., Price P. A., Fox D. B., 2006a, GRB Coordinates Network, 4622
Berger E., Kulkarni S. R., Rau A., Fox D. B., 2006b, GRB Coordinates Network, 4815
Berger E., Cenko S. B., Rau A., 2006c, GRB Coordinates Network, 5071
Berger E., Morrell N., Roth M., 2007a, GRB Coordinates Network, 7151
Berger E., Morrell N., Roth M., 2007b, GRB Coordinates Network, 7154
Berger E., Fox D. B., Cucchiara A., Cenko S. B., 2008, GRB Coordinates Network, 8335
Bissaldi E., McBreen S., 2008, GRB Coordinates Network, 8715
Bloom J. S., Nugent P. E., 2010, GRB Coordinates Network, 10433
Bloom J. S., Kulkarni S. R., Djorgovski S. G., 2002, AJ, 123, 1111
Bloom J. S., Frail D. A., Kulkarni S. R., 2003, ApJ, 594, 674
Bloom J. S., Perley D., Foley R., Prochaska J. X., Chen H. W., Starr D., 2005, GRB Coordinates Network, 3758
Bloom J. S., Foley R. J., Koceveki D., Perley D., 2006a, GRB Coordinates Network, 5217
Bloom J. S., Perley D., Kocevski D., Butler N., Prochaska J. X., Chen H.-W., 2006b, GRB Coordinates Network, 5238
Bolatto A. D., Leroy A. K., Rosolowsky E., Walter F., Blitz L., 2008, ApJ, 686, 948
Bolmer J., Graham J., Knust F., Greiner J., 2015a, GRB Coordinates Network, 18598
Bolmer J., Knust F., Greiner J., 2015b, GRB Coordinates Network, 18603
Boquien M., et al., 2013, A&A, 554, A14
Brightman M., Nandra K., 2011, MNRAS, 413, 1206
Brüns C., et al., 2005, A&A, 432, 45
Buchner J., et al., 2014, A&A, 564, A125
Buchner J., et al., 2015, ApJ, 802, 89
Burrows D. N., et al., 2005, Space Sci. Rev., 120, 165
Butler N. R., Bloom J. S., Poznanski D., 2010, ApJ, 711, 495
Campana S., 2015, GRB Coordinates Network, 18483
Campana S., et al., 2006, A&A, 449, 61
Campana S., Thöne C. C., de Ugarte Postigo A., Tagliaferri G., Moretti A., Covino S., 2010a, MNRAS, 402, 2429
Campana S., Starling R. L. C., Evans P. A., Sakamoto T., 2010b, GRB Coordinates Network, 11195
Campana S., D'Avanzo P., Lazzati D., Covino S., Tagliaferri G., Panagia N., 2011, MNRAS, 418, 1511
Campana S., et al., 2012, MNRAS, 421, 1697

Cano Z., et al., 2013, GRB Coordinates Network, 15445
Cash W., 1979, ApJ, 228, 939
Castro-Tirado A. J., Amado P., Negueruela I., Gorosabel J., Jelinek M., de Ugarte Postigo A., 2006, GRB Coordinates Network, 5218
Castro-Tirado A. J., et al., 2014a, GRB Coordinates Network, 16505
Castro-Tirado A. J., Gorosabel J., Garcia-Rodriguez A., 2014b, GRB Coordinates Network, 16797
Castro-Tirado A. J., Sanchez-Ramirez R., Gorosabel J., Scarpa R., 2015a, GRB Coordinates Network, 17278
Castro-Tirado A. J., Sanchez-Ramirez R., Lombardi G., Rivero M. A., 2015b, GRB Coordinates Network, 17758
Cenko S. B., Baumgartner W. H., 2006, GRB Coordinates Network, 5156
Cenko S. B., Berger E., Cohen J., 2006a, GRB Coordinates Network, 4592
Cenko S. B., Berger E., Djorgovski S. G., Mahabal A. A., Fox D. B., 2006b, GRB Coordinates Network, 5155
Cenko S. B., Ofek E. O., Gelino D., Thompson T., Price P. A., Berger E., 2006c, GRB Coordinates Network, 5457
Cenko S. B., Kasliwal M. M., Kulkarni S. R., 2009, GRB Coordinates Network, 10093
Cenko S. B., Bloom J. S., Perley D. A., Cobb B. E., 2010a, GRB Coordinates Network, 10443
Cenko S. B., Perley D. A., Morgan A. N., Klein C. R., Bloom J. S., Butler N. R., Cobb B. E., 2010b, GRB Coordinates Network, 10752
Cenko S. B., Levan A. J., Chornock R., Berger E., Perley D. A., Bloom J. S., Tanvir N., 2010c, GRB Coordinates Network, 11468
Cenko S. B., Hora J. L., Bloom J. S., 2011, GRB Coordinates Network, 11638
Chen H.-W., Thompson I., Prochaska J. X., Bloom J., 2005, GRB Coordinates Network, 3709
Chen H.-W., Helsby J., Shectman S., Thompson I., Crane J., 2009, GRB Coordinates Network, 10038
Chornock R., Berger E., 2011, GRB Coordinates Network, 11518
Chornock R., Fong W., 2015, GRB Coordinates Network, 17358
Chornock R., Fong W., Berger E., Persson E., 2010, GRB Coordinates Network, 11469
Chornock R., Lunnan R., Berger E., 2013, GRB Coordinates Network, 15307
Chornock R., Fox D. B., Tanvir N. R., Berger E., 2014a, GRB Coordinates Network, 15966
Chornock R., Fox D. B., Berger E., 2014b, GRB Coordinates Network, 16269
Chornock R., Fox D. B., Cucchiara A., Perley D. A., Levan A., 2014c, GRB Coordinates Network, 16301
Chornock R., Fong W., Fox D. B., 2014d, GRB Coordinates Network, 17177
Cobb B. E., Bailyn C. D., 2006, GRB Coordinates Network, 5282
Collazzi A. C., Connaughton V., 2013, GRB Coordinates Network, 14972
Connaughton V., 2009, GRB Coordinates Network, 9230
Croton D. J., et al., 2006, MNRAS, 365, 11
Croton D. J., et al., 2016, preprint, (arXiv:1601.04709)
Cucchiara A., Cenko S. B., 2013a, GRB Coordinates Network, 14687
Cucchiara A., Cenko S. B., 2013b, GRB Coordinates Network, 15624
Cucchiara A., Fox D. B., 2008, GRB Coordinates Network, 8304
Cucchiara A., Fox D. B., 2010, GRB Coordinates Network, 10624
Cucchiara A., Perley D., 2013, GRB Coordinates Network, 15144
Cucchiara A., Prochaska J. X., 2012, GRB Coordinates Network, 12865
Cucchiara A., Tanvir N. R., 2013, GRB Coordinates Network, 14621
Cucchiara A., Fox D. B., Berger E., 2006a, GRB Coordinates Network, 4729
Cucchiara A., Price P. A., Fox D. B., Cenko S. B., Schmidt B. P., 2006b, GRB Coordinates Network, 5052
Cucchiara A., Fox D. B., Cenko S. B., Berger E., Price P. A., Radomski J., 2007, GRB Coordinates Network, 6665
Cucchiara A., Fox D. B., Cenko S. B., 2008a, GRB Coordinates Network, 7615
Cucchiara A., Fox D. B., Cenko S. B., Berger E., 2008b, GRB Coordinates Network, 8448
Cucchiara A., Fox D., Tanvir N., 2009a, GRB Coordinates Network, 10065

---

[10] https://johannesbuchner.github.io/BXA/
[11] https://johannesbuchner.github.io/PyMultiNest/
[12] http://roban.github.com/CosmoloPy/

Cucchiara A., Fox D., Levan A., Tanvir N., 2009b, GRB Coordinates Network, 10202

Cucchiara A., Perley D., Cenko S. B., 2013, GRB Coordinates Network, 14748

Cucchiara A., Cenko S. B., Perley D. A., Capone J., Toy V., 2014, GRB Coordinates Network, 16774

Cummings J. R., et al., 2009, GRB Coordinates Network, 9139

Curran P. A., Evans P. A., de Pasquale M., Page M. J., van der Horst A. J., 2010, ApJ, 716, L135

D'Avanzo P., Fiore F., Piranomonte S., Covino S., Tagliaferri G., Chincarini G., Stella L., 2007, GRB Coordinates Network, 7152

D'Avanzo P., D'Elia V., di Fabrizio L., Gurtu A., 2011a, GRB Coordinates Network, 11997

D'Avanzo P., et al., 2011b, GRB Coordinates Network, 12284

D'Avanzo P., D'Elia V., Piranomonte S., Melandri A., Malesani D., Pursimo T., Baglio M. C., Andreoni I., 2014, GRB Coordinates Network, 15964

D'Elia V., et al., 2005a, GRB Coordinates Network, 3746

D'Elia V., et al., 2005b, GRB Coordinates Network, 4044

D'Elia V., Covino S., D'Avanzo P., 2008, GRB Coordinates Network, 8438

D'Elia V., D'Avanzo P., Malesani D., di Fabrizio L., Tessicini G., 2013, GRB Coordinates Network, 15310

D'Elia V., et al., 2015a, GRB Coordinates Network, 18187

D'Elia V., Kruehler T., Xu D., Jakobsson P., Tanvir N. R., de Ugarte Postigo A., 2015b, GRB Coordinates Network, 18318

D'Elia V., Melandri A., Antonelli L. A., Malesani D., 2016, GRB Coordinates Network, 18915

Dereli H., Boer M., Gendre B., Amati L., Dichiara S., 2015, preprint, (arXiv:1506.05521)

Dickey J. M., Lockman F. J., 1990, ARA&A, 28, 215

Dupree A. K., Falco E., Prochaska J. X., Chen H.-W., Bloom J. S., 2006, GRB Coordinates Network, 4969

Elliott J., Schady P., Kann D. A., Greiner J., 2012, GRB Coordinates Network, 13457

Evans P. A., et al., 2009, MNRAS, 397, 1177

Evans P. A., et al., 2010, A&A, 519, A102

Evans P. A., et al., 2014, MNRAS, 444, 250

Fatkhullin T. A., Sokolov V. V., Moiseev A. V., Guziy S., Castro-Tirado A. J., 2006, GRB Coordinates Network, 4809

Feroz F., Hobson M. P., Bridges M., 2009, MNRAS, 398, 1601

Feroz F., Hobson M. P., Cameron E., Pettitt A. N., 2013, preprint, (arXiv:1306.2144)

Ferrero P., et al., 2006, GRB Coordinates Network, 5489

Fitzpatrick G., Jenke P., 2013, GRB Coordinates Network, 15455

Flores H., et al., 2010, GRB Coordinates Network, 11317

Flores H., et al., 2013a, GRB Coordinates Network, 14491

Flores H., Covino S., de Ugarte Postigo A., Fynbo J., Kruehler T., Xu D., Tanvir N., 2013b, GRB Coordinates Network, 14493

Foley R. J., Chen H.-W., Bloom J. S., Prochaska J. X., 2005, GRB Coordinates Network, 3949

Foley R. J., Bloom J. S., Perley D. A., Butler N. R., 2006, GRB Coordinates Network, 5376

Fontanot F., De Lucia G., Monaco P., Somerville R. S., Santini P., 2009, MNRAS, 397, 1776

Freeman P., Doe S., Siemiginowska A., 2001, in Starck J.-L., Murtagh F. D., eds, Society of Photo-Optical Instrumentation Engineers (SPIE) Conference Series Vol. 4477, Society of Photo-Optical Instrumentation Engineers (SPIE) Conference Series. pp 76–87 (arXiv:astro-ph/0108426), doi:10.1117/12.447161

Fruchter A. S., et al., 2006, Nature, 441, 463

Fugazza D., et al., 2005, GRB Coordinates Network, 3948

Fugazza D., et al., 2006a, GRB Coordinates Network, 5276

Fugazza D., et al., 2006b, GRB Coordinates Network, 5513

Fynbo J. P. U., et al., 2005a, GRB Coordinates Network, 3749

Fynbo J. P. U., et al., 2005b, GRB Coordinates Network, 3874

Fynbo J. P. U., Jensen B. L., Castro Cerón J. M., Naeraenen J., 2006a, GRB Coordinates Network, 4686

Fynbo J. P. U., Limousin M., Castro Cerón J. M., Jensen B. L., Naranen J., 2006b, GRB Coordinates Network, 4692

Fynbo J. P. U., et al., 2006c, GRB Coordinates Network, 5277

Fynbo J. P. U., et al., 2009, ApJS, 185, 526

Fynbo J. P. U., de Ugarte Postigo A., D'Elia V., Xu D., Malesani D., 2012, GRB Coordinates Network, 13477

Fynbo J. P. U., Tanvir N. R., Jakobsson P., Xu D., Malesani D., Milvang-Jensen B., 2014, GRB Coordinates Network, 16217

Garnavich P., 2013, GRB Coordinates Network, 14605

Gehrels N., 2004, in Fenimore E., Galassi M., eds, American Institute of Physics Conference Series Vol. 727, Gamma-Ray Bursts: 30 Years of Discovery. pp 637–641 (arXiv:astro-ph/0405233), doi:10.1063/1.1810924

Genel S., et al., 2014, MNRAS, 445, 175

Giuliani A., Mereghetti S., 2014, A&A, 563, A6

Golenetskii S., Aptekar R., Mazets E., Pal'Shin V., Frederiks D., Cline T., 2005a, GRB Coordinates Network, 3179

Golenetskii S., Aptekar R., Mazets E., Pal'Shin V., Frederiks D., Cline T., 2005b, GRB Coordinates Network, 3518

Golenetskii S., Aptekar R., Mazets E., Pal'Shin V., Frederiks D., Cline T., 2005c, GRB Coordinates Network, 4030

Golenetskii S., Aptekar R., Mazets E., Pal'Shin V., Frederiks D., Cline T., 2005d, GRB Coordinates Network, 4150

Golenetskii S., Aptekar R., Mazets E., Pal'Shin V., Frederiks D., Cline T., 2005e, GRB Coordinates Network, 4238

Golenetskii S., Aptekar R., Mazets E., Pal'Shin V., Frederiks D., Ulanov M., Cline T., 2006a, GRB Coordinates Network, 4989

Golenetskii S., Aptekar R., Mazets E., Pal'Shin V., Frederiks D., Cline T., 2006b, GRB Coordinates Network, 5264

Golenetskii S., Aptekar R., Mazets E., Pal'Shin V., Frederiks D., Cline T., 2006c, GRB Coordinates Network, 5460

Golenetskii S., Aptekar R., Mazets E., Pal'Shin V., Frederiks D., Cline T., 2006d, GRB Coordinates Network, 5748

Golenetskii S., Aptekar R., Mazets E., Pal'Shin V., Frederiks D., Cline T., 2006e, GRB Coordinates Network, 5837

Golenetskii S., Aptekar R., Mazets E., Pal'Shin V., Frederiks D., Cline T., 2007a, GRB Coordinates Network, 6230

Golenetskii S., Aptekar R., Mazets E., Pal'Shin V., Frederiks D., Oleynik P., Ulanov M., Cline T., 2007b, GRB Coordinates Network, 6403

Golenetskii S., Aptekar R., Mazets E., Pal'Shin V., Frederiks D., Cline T., 2007c, GRB Coordinates Network, 6459

Golenetskii S., Aptekar R., Mazets E., Pal'Shin V., Frederiks D., Cline T., 2007d, GRB Coordinates Network, 6849

Golenetskii S., Aptekar R., Mazets E., Pal'Shin V., Frederiks D., Cline T., 2007e, GRB Coordinates Network, 6960

Golenetskii S., Aptekar R., Mazets E., Pal'Shin V., Frederiks D., Cline T., 2008a, GRB Coordinates Network, 7487

Golenetskii S., Aptekar R., Mazets E., Pal'Shin V., Frederiks D., Cline T., 2008b, GRB Coordinates Network, 7589

Golenetskii S., Aptekar R., Mazets E., Pal'Shin V., Frederiks D., Cline T., 2008c, GRB Coordinates Network, 7784

Golenetskii S., Aptekar R., Mazets E., Pal'Shin V., Frederiks D., Cline T., 2008d, GRB Coordinates Network, 7854

Golenetskii S., et al., 2008e, GRB Coordinates Network, 8259

Golenetskii S., et al., 2008f, GRB Coordinates Network, 8548

Golenetskii S., et al., 2008g, GRB Coordinates Network, 8694

Golenetskii S., et al., 2009a, GRB Coordinates Network, 8776

Golenetskii S., et al., 2009b, GRB Coordinates Network, 9553

Golenetskii S., Aptekar R., Mazets E., Pal'Shin V., Frederiks D., Oleynik P., Ulanov M., Svinkin D., 2009c, GRB Coordinates Network, 9647

Golenetskii S., et al., 2009d, GRB Coordinates Network, 9679

Golenetskii S., et al., 2009e, GRB Coordinates Network, 10057

Golenetskii S., et al., 2010a, GRB Coordinates Network, 10882

Golenetskii S., et al., 2010b, GRB Coordinates Network, 11119

Golenetskii S., et al., 2011a, GRB Coordinates Network, 11659

Golenetskii S., et al., 2011b, GRB Coordinates Network, 11723

Golenetskii S., et al., 2011c, GRB Coordinates Network, 11971

Golenetskii S., et al., 2011d, GRB Coordinates Network, 12008

Golenetskii S., et al., 2011e, GRB Coordinates Network, 12166

Golenetskii S., et al., 2011f, GRB Coordinates Network, 12223

Golenetskii S., et al., 2011g, GRB Coordinates Network, 12433
Golenetskii S., et al., 2011h, GRB Coordinates Network, 12663
Golenetskii S., et al., 2012a, GRB Coordinates Network, 12872
Golenetskii S., et al., 2012b, GRB Coordinates Network, 13736
Golenetskii S., et al., 2012c, GRB Coordinates Network, 14010
Golenetskii S., et al., 2013a, GRB Coordinates Network, 14368
Golenetskii S., et al., 2013b, GRB Coordinates Network, 14417
Golenetskii S., et al., 2013c, GRB Coordinates Network, 14487
Golenetskii S., et al., 2013d, GRB Coordinates Network, 14808
Golenetskii S., Aptekar R., Frederiks D., Pal'Shin V., Oleynik P., Ulanov M., Svinkin D., Cline T., 2013e, GRB Coordinates Network, 14958
Golenetskii S., Aptekar R., Frederiks D., Pal'Shin V., Oleynik P., Ulanov M., Svinkin D., Cline T., 2013f, GRB Coordinates Network, 15145
Golenetskii S., Aptekar R., Frederiks D., Pal'Shin V., Oleynik P., Ulanov M., Svinkin D., Cline T., 2013g, GRB Coordinates Network, 15203
Golenetskii S., Aptekar R., Frederiks D., Pal'Shin V., Oleynik P., Ulanov M., Svinkin D., Cline T., 2013h, GRB Coordinates Network, 15260
Golenetskii S., Aptekar R., Frederiks D., Pal'Shin V., Oleynik P., Ulanov M., Svinkin D., Cline T., 2013i, GRB Coordinates Network, 15413
Golenetskii S., Aptekar R., Frederiks D., Pal'Shin V., Oleynik P., Ulanov M., Svinkin D., Cline T., 2014a, GRB Coordinates Network, 15670
Golenetskii S., et al., 2014b, GRB Coordinates Network, 16495
Gorosabel J., de Ugarte Postigo A., Thoene C. C., Tanvir N., Fynbo J. P. U., Garcia-Alvarez D., Perez-Romero A., 2014, GRB Coordinates Network, 17234
Graham J. F., Fruchter A. S., 2013, ApJ, 774, 119
Grazian A., et al., 2006, GRB Coordinates Network, 4545
Greiner J., et al., 2011, A&A, 526, A30
Greiner J., et al., 2015, ApJ, 809, 76
Groot P., et al., 2010, GRB Coordinates Network, 10441
Gruber D., 2010, GRB Coordinates Network, 11248
Gruber D., 2012, GRB Coordinates Network, 13469
Gruber D., Pelassa V., 2012, GRB Coordinates Network, 13437
Gruber D., et al., 2014, ApJS, 211, 12
Halpern J. P., Mirabal N., 2006a, GRB Coordinates Network, 4749
Halpern J. P., Mirabal N., 2006b, GRB Coordinates Network, 5072
Halpern J. P., Mirabal N., 2006c, GRB Coordinates Network, 5982
Hartoog O. E., Malesani D., Wiersema K., Kruehler T., Schulze S., de Ugarte Postigo A., D'Elia V., Fynbo J. P. U., 2012, GRB Coordinates Network, 13730
Hartoog O. E., Xu D., Malesani D., Tanvir N. R., Fynbo J. P. U., Kaper L., D'Elia V., 2013, GRB Coordinates Network, 15494
Hartoog O. E., Malesani D., Sanchez-Ramirez R., de Ugarte Postigo A., Levan A. J., Fynbo J. P. U., Vreeswijk P. M., Kaper L., 2014, GRB Coordinates Network, 16437
Hearty F., Bayliss M., Lamb D. Q., McMillan R., Ketzeback B., Barentine J., Dembicky J., York D. G., 2006, GRB Coordinates Network, 4753
Hill G., Prochaska J. X., Fox D., Schaefer B., Reed M., 2005, GRB Coordinates Network, 4255
Hjorth J., Bloom J. S., 2012, The Gamma-Ray Burst - Supernova Connection. pp 169–190, http://arxiv.org/pdf/1104.2274v1
Holland S., 2008, GRB Coordinates Network, 8212
Holland S. T., Kuin N. P. M., Rowlinson A., 2010, GRB Coordinates Network, 10432
Hurley K., et al., 2007, GRB Coordinates Network, 6024
Jakobsson P., Fynbo J. P. U., Paraficz D., Telting J., Jensen B. L., Hjorth J., Castro Cerón J. M., 2005a, GRB Coordinates Network, 4017
Jakobsson P., Fynbo J. P. U., Paraficz D., Telting J., Jensen B. L., Hjorth J., Castro Cerón J. M., 2005b, GRB Coordinates Network, 4029
Jakobsson P., et al., 2006a, A&A, 447, 897
Jakobsson P., Tanvir N., Jensen B. L., Fynbo J. P. U., de Ugarte Postigo A., Gorosabel J., Klose S., Vreeswijk P., 2006b, GRB Coordinates Network, 5298
Jakobsson P., et al., 2006c, GRB Coordinates Network, 5319
Jakobsson P., Vreeswijk P., Fynbo J. P. U., Hjorth J., Starling R., Kann D. A., Hartmann D., 2006d, GRB Coordinates Network, 5320
Jakobsson P., Fynbo J. P. U., Hjorth J., Tanvir N., Gorosabel J., Nielsen T. B., Holhjem K., 2006e, GRB Coordinates Network, 5337

Jakobsson P., Levan A., Chapman R., Rol E., Tanvir N., Vreeswijk P., Watson D., 2006f, GRB Coordinates Network, 5617
Jakobsson P., Malesani D., Fynbo J. P. U., Hjorth J., Vreeswijk P. M., Tanvir N. R., 2007, GRB Coordinates Network, 6997
Jakobsson P., et al., 2012, ApJ, 752, 62
Jenke P., 2012, GRB Coordinates Network, 13642
Jenke P., 2014, GRB Coordinates Network, 16220
Jenke P., Burns E., 2015, GRB Coordinates Network, 17988
Jensen B. L., et al., 2005, GRB Coordinates Network, 3809
Jeong S., et al., 2014a, GRB Coordinates Network, 15922
Jeong S., Sanchez-Ramirez R., Gorosabel J., Castro-Tirado A. J., 2014b, GRB Coordinates Network, 15936
Kalberla P. M. W., Burton W. B., Hartmann D., Arnal E. M., Bajaja E., Morras R., Pöppel W. G. L., 2005, A&A, 440, 775
Kelly B. C., Fan X., Vestergaard M., 2008, ApJ, 682, 874
Kelly P. L., Filippenko A. V., Fox O. D., Zheng W., Clubb K. I., 2013, ApJ, 775, L5
Knust F., Kruehler T., Klose S., Greiner J., 2012, GRB Coordinates Network, 13810
Krimm H., et al., 2007, GRB Coordinates Network, 7081
Krimm H. A., et al., 2010, GRB Coordinates Network, 10670
Krimm H. A., et al., 2012, GRB Coordinates Network, 13137
Kruehler T., Nicuesa A., Klose S., Greiner J., Afonso P., 2010, GRB Coordinates Network, 10439
Kruehler T., Fynbo J. P. U., Milvang-Jensen B., Tanvir N., Jakobsson P., 2012a, GRB Coordinates Network, 13134
Kruehler T., et al., 2012b, GRB Coordinates Network, 13930
Kruehler T., Xu D., Sanchez-Ramirez R., Malesani D., Fynbo J., Flores H., 2013, GRB Coordinates Network, 14390
Kruehler T., Malesani D., de Ugarte Postigo A., Melandri A., Fynbo J. P. U., 2014a, GRB Coordinates Network, 16194
Kruehler T., Vreeswijk P. M., Fynbo J. P. U., 2014b, GRB Coordinates Network, 16401
Kruehler T., Xu D., Fynbo J. P. U., Malesani D., Cano Z., de Ugarte Postigo A., 2015, GRB Coordinates Network, 17420
Krühler T., 2015, Astronomische Nachrichten, 336, 487
Krühler T., et al., 2011, A&A, 534, A108
Krühler T., et al., 2012, ApJ, 758, 46
Kuin N. P. M., Gelbord J. M., 2011, GRB Coordinates Network, 11575
Landsman W., de Pasquale M., Kuin P., Schady P., Smith P., Parsons A., 2008, GRB Coordinates Network, 8601
Larson R. B., 1981, MNRAS, 194, 809
Laskar T., Zauderer A., Berger E., 2012, GRB Coordinates Network, 13903
Ledoux C., et al., 2005, GRB Coordinates Network, 3860
Ledoux C., Vreeswijk P., Smette A., Jaunsen A., Kaufer A., 2006, GRB Coordinates Network, 5237
Levan A. J., Jakobsson P., Chapman R., Tanvir N., Rol E., 2006, GRB Coordinates Network, 5573
Levan A. J., Wiersema K., Tanvir N. R., 2011, GRB Coordinates Network, 12429
Levan A. J., Cenko S. B., Perley D. A., Tanvir N. R., 2013, GRB Coordinates Network, 14455
Levesque E., Chornock R., Kewley L., Bloom J. S., Prochaska J. X., Perley D. A., Cenko S. B., Modjaz M., 2009, GRB Coordinates Network, 9264
Lombardi M., Alves J., Lada C. J., 2010, A&A, 519, L7
Loredo T. J., 2004, in R. Fischer, R. Preuss, & U. V. Toussaint ed., American Institute of Physics Conference Series Vol. 735, American Institute of Physics Conference Series. pp 195–206 (arXiv:astro-ph/0409387), doi:10.1063/1.1835214, http://scitation.aip.org/content/aip/proceeding/aipcp/10.1063/1.1835214
Lu Y., Mo H. J., Lu Z., 2015, preprint, (arXiv:1504.02109)
Madau P., Dickinson M., 2014, ARA&A, 52, 415
Malesani D., 2006, GRB Coordinates Network, 5456
Malesani D., 2010, GRB Coordinates Network, 10621
Malesani D., Fynbo J. P. U., Christensen L., de Ugarte Postigo A., Milvang-Jensen B., Covino S., 2009, GRB Coordinates Network, 9761
Malesani D., et al., 2015a, GRB Coordinates Network, 17755

Malesani D., Tanvir N. R., Kruehler T., de Ugarte Postigo A., Flores H., Xu D., Fynbo J. P. U., 2015b, GRB Coordinates Network, 18540

Malesani D., D'Elia V., D'Avanzo P., Melandri A., Antonelli L. A., di Fabrizio L., Mainella G., 2016, GRB Coordinates Network, 18965

Markwardt C. B., et al., 2009, GRB Coordinates Network, 10040

Marshall H. L., Tananbaum H., Avni Y., Zamorani G., 1983, ApJ, 269, 35

Martin-Carrillo A., et al., 2014, A&A, 567, A84

Masetti N., Palazzi E., Pian E., Patat F., 2006, GRB Coordinates Network, 4803

McBreen S., 2009a, GRB Coordinates Network, 9415

McBreen S., 2009b, GRB Coordinates Network, 10266

McMillan P. J., 2011, MNRAS, 414, 2446

Meidt S. E., et al., 2014, ApJ, 788, 144

Melandri A., Grazian A., Guidorzi C., Monfardini A., Mundell C. G., Gomboc A., 2006, GRB Coordinates Network, 4539

Milisavljevic D., Drout M., Berger E., 2012, GRB Coordinates Network, 12867

Mirabal N., 2006, GRB Coordinates Network, 4783

Mirabal N., Halpern J. P., 2006a, GRB Coordinates Network, 4591

Mirabal N., Halpern J. P., 2006b, GRB Coordinates Network, 4792

Oates S. R., Morris D. C., 2010, GRB Coordinates Network, 11026

Ofek E. O., Cenko S. B., Gal-Yam A., Peterson B., Schmidt B. P., Fox D. B., Price P. A., 2006, GRB Coordinates Network, 5123

Onda K., et al., 2006, GRB Coordinates Network, 5907

Pagani C., et al., 2007, in Society of Photo-Optical Instrumentation Engineers (SPIE) Conference Series. p. 9, doi:10.1117/12.734398, http://www.iasf-palermo.inaf.it/~cusumano/conferen/PSI668609.pdf

Pal'Shin V., 2006, GRB Coordinates Network, 5984

Pal'Shin V., et al., 2009a, GRB Coordinates Network, 9196

Pal'Shin V., et al., 2009b, GRB Coordinates Network, 9821

Pancoast A., Rosen R., Bennert V., Cucchiara A., Prochaska J. X., 2012, GRB Coordinates Network, 12866

Perley D. A., 2014, GRB Coordinates Network, 16181

Perley D. A., Cenko S. B., 2015, GRB Coordinates Network, 17616

Perley D. A., Tanvir N. R., 2012, GRB Coordinates Network, 13133

Perley D. A., Foley R. J., Bloom J. S., Butler N. R., 2006, GRB Coordinates Network, 5387

Perley D. A., Chornock R., Bloom J. S., 2008a, GRB Coordinates Network, 7962

Perley D. A., Bloom J. S., Kalirai J., Strickler R., Ramirez-Ruiz E., Miller A. A., 2008b, GRB Coordinates Network, 8711

Perley D. A., Berger E., Cenko S. B., Chornock R., Levan A. J., Tanvir N., 2010, GRB Coordinates Network, 11464

Perley D. A., et al., 2011, AJ, 141, 36

Perley D. A., et al., 2013, ApJ, 778, 128

Perley D. A., Ott C. P., Modjaz M., Fierroz D., 2014a, GRB Coordinates Network, 17081

Perley D. A., Cao Y., Cenko S. B., 2014b, GRB Coordinates Network, 17228

Perley D. A., Hillenbrand L., Prochaska J. X., 2015, GRB Coordinates Network, 18487

Perley D. A., Niino Y., Tanvir N. R., Vergani S. D., Fynbo J. P. U., 2016a, Space Sci. Rev.,

Perley D. A., et al., 2016b, ApJ, 817, 7

Perley D. A., et al., 2016c, ApJ, 817, 8

Peterson B., Schmidt B., 2006, GRB Coordinates Network, 5223

Piran T., 2005, Rev. Mod. Phys., 76, 1143

Piranomonte S., et al., 2005, GRB Coordinates Network, 4032

Piranomonte S., et al., 2006a, GRB Coordinates Network, 4520

Piranomonte S., et al., 2006b, GRB Coordinates Network, 4583

Price P. A., 2006, GRB Coordinates Network, 5104

Price P. A., Berger E., Fox D. B., Cenko S. B., Rau A., 2006a, GRB Coordinates Network, 5077

Price P. A., Berger E., Fox D. B., 2006b, GRB Coordinates Network, 5275

Prochaska J. X., 2005, GRB Coordinates Network, 4271

Prochaska J. X., Chen H.-W., Bloom J. S., O'Meara J., Burles S. M., Thompson I., 2005a, GRB Coordinates Network, 3732

Prochaska J. X., Bloom J. S., Wright J. T., Butler R. P., Chen H. W., Vogt S. S., Marcy G. W., 2005b, GRB Coordinates Network, 3833

Prochaska J. X., Foley R. J., Chen H.-W., Bloom J. S., Hurley K., Cooper M., Guhathakurta R., Li W., 2005c, GRB Coordinates Network, 3971

Prochaska J. X., Foley R., Tran H., Bloom J. S., Chen H.-W., 2006a, GRB Coordinates Network, 4593

Prochaska J. X., Wong D. S., Park S.-H., Filippenko A. V., Foley R. J., Li W., 2006b, GRB Coordinates Network, 4701

Prochaska J. X., Chen H.-W., Bloom J. S., Falco E., Dupree A. K., 2006c, GRB Coordinates Network, 5002

Prochaska J. X., Murphy M., Malec A. L., Miller K., 2008a, GRB Coordinates Network, 7388

Prochaska J. X., Foley R. J., Holden B., Magee D., Cooper M., Dutton A., 2008b, GRB Coordinates Network, 7397

Pugliese V., Xu D., Tanvir N. R., Wiersema K., Fynbo J. P. U., Milvang-Jensen B., D'Elia V., 2015, GRB Coordinates Network, 17672

Pugliese G., Covino S., Kruehler T., Xu D., Tanvir N. R., 2016, GRB Coordinates Network, 18982

Quimby R., Fox D., Hoeflich P., Roman B., Wheeler J. C., 2005, GRB Coordinates Network, 4221

Reichart D. E., 2001, ApJ, 553, 235

Reichart D. E., Price P. A., 2002, ApJ, 565, 174

Rol E., et al., 2005, GRB Coordinates Network, 3710

Rol E., Jakobsson P., Tanvir N., Levan A., 2006, GRB Coordinates Network, 5555

Romano P., et al., 2006, A&A, 456, 917

Rossi A., et al., 2011, A&A, 529, A142

Sakamoto T., et al., 2008a, ApJS, 175, 179

Sakamoto T., et al., 2008b, GRB Coordinates Network, 8101

Sakamoto T., et al., 2009, ApJ, 693, 922

Sakamoto T., et al., 2010, GRB Coordinates Network, 11169

Sakamoto T., et al., 2011, GRB Coordinates Network, 12276

Sanchez-Ramirez R., Gorosabel J., Castro-Tirado A. J., Rivero M. A., Gomez-Velarde G., 2012a, GRB Coordinates Network, 13146

Sanchez-Ramirez R., Gorosabel J., de Ugarte Postigo A., Gonzalez Perez J. M., 2012b, GRB Coordinates Network, 13723

Sanchez-Ramirez R., Gorosabel J., Castro-Tirado A. J., Cepa J., Gomez-Velarde G., 2013a, GRB Coordinates Network, 14685

Sanchez-Ramirez R., et al., 2013b, GRB Coordinates Network, 14747

Sanchez-Ramirez R., Castro-Tirado A. J., Hoyos F., Aceituno J., 2015a, GRB Coordinates Network, 17697

Sanchez-Ramirez R., et al., 2015b, GRB Coordinates Network, 18177

Sanchez-Ramirez R., Oates S. R., Tello J. C., Geier S., Tristam P., Castro-Tirado A. J., 2016, GRB Coordinates Network, 18925

Savaglio S., Palazzi E., Ferrero P., Klose S., 2007, GRB Coordinates Network, 6166

Schady P., Savaglio S., Krühler T., Greiner J., Rau A., 2011, A&A, 525, A113

Schady P., et al., 2015, A&A, 579, A126

Schulze S., et al., 2012, GRB Coordinates Network, 13257

Schulze S., Wiersema K., Xu D., Fynbo J. P. U., 2014a, GRB Coordinates Network, 15831

Schulze S., Kruehler T., Xu D., Fynbo J. P. U., Tanvir N. R., Jakobsson P., Galleti S., 2014b, GRB Coordinates Network, 16891

Schulze S., et al., 2015, ApJ, 808, 73

Smette A., Ledoux C., Vreeswijk P., De Cia A., Petitjean P., Fynbo J., Malesani D., Fox A., 2013, GRB Coordinates Network, 14848

Soderberg A. M., Berger E., 2005, GRB Coordinates Network, 4375

Soderberg A. M., Berger E., Ofek E., 2005, GRB Coordinates Network, 4186

Soderberg A. M., Berger E., Schmidt B. P., 2006, GRB Coordinates Network, 4804

Sokolov V. V., et al., 2013, GRB Coordinates Network, 14669

Stanbro M., 2014, GRB Coordinates Network, 16262

Still A., et al., 2006, GRB Coordinates Network, 5226

Tacconi L. J., et al., 2013, ApJ, 768, 74

Tanga M., Schmidl S., Klose S., Varela K., Greiner J., 2013, GRB Coordinates Network, 15493

Tanvir N. R., Wiersema K., Levan A. J., 2010, GRB Coordinates Network, 11230

Tanvir N. R., Levan A. J., Cucchiara A., Fox D. B., 2012a, GRB Coordinates Network, 13251

Tanvir N. R., et al., 2012b, GRB Coordinates Network, 13348

Tanvir N. R., Levan A. J., Krogsrud D., 2012c, GRB Coordinates Network, 13458

Tanvir N. R., Fynbo J. P. U., Melandri A., Levan A. J., Xu D., D'Elia V., 2012d, GRB Coordinates Network, 13890

Tanvir N. R., Wiersema K., Levan A. J., Starling R. L. C., Margheim S., Hayward T., 2012e, GRB Coordinates Network, 13929

Tanvir N. R., Wiersema K., Xu D., Fynbo J. P. U., 2013, GRB Coordinates Network, 14882

Tanvir N. R., Levan A. J., Wiersema K., Cucchiara A., 2014a, GRB Coordinates Network, 15961

Tanvir N. R., Levan A. J., Coulson D., 2014b, GRB Coordinates Network, 16570

Tanvir N. R., Kruehler T., Malesani D., Xu D., de Ugarte Postigo A., Pugliese G., 2015, GRB Coordinates Network, 18524

Tchernyshyov K., Meixner M., Seale J., Fox A., Friedman S. D., Dwek E., Galliano F., 2015, ApJ, 811, 78

Thoene C. C., Fynbo J. P. U., Sollerman J., Jensen B. L., Hjorth J., Jakobsson P., Klose S., 2006a, GRB Coordinates Network, 5161

Thoene C. C., et al., 2006b, GRB Coordinates Network, 5373

Thoene C. C., Henriksen C., Wiersema K., 2006c, GRB Coordinates Network, 5674

Thoene C. C., Perley D. A., Bloom J. S., 2007a, GRB Coordinates Network, 6663

Thoene C. C., Perley D. A., Cooke J., Bloom J. S., Chen H.-W., Barton E., 2007b, GRB Coordinates Network, 6741

Thoene C. C., et al., 2009a, GRB Coordinates Network, 9269

Thoene C. C., et al., 2009b, GRB Coordinates Network, 10233

Thoene C. C., de Ugarte Postigo A., Vreeswijk P., D'Avanzo P., Covino S., Fynbo J. P. U., Tanvir N., 2010, GRB Coordinates Network, 10971

Thone C., et al., 2005, GRB Coordinates Network, 4291

Thone C. C., de Ugarte Postigo A., Gorosabel J., Tanvir N., Fynbo J. P. U., 2013, GRB Coordinates Network, 14744

Toy V. L., et al., 2016, ApJ, 818, 79

Ueda Y., Akiyama M., Hasinger G., Miyaji T., Watson M. G., 2014, ApJ, 786, 104

Veres P., Corsi A., Frail D. A., Cenko S. B., Perley D. A., 2015, ApJ, 810, 31

Vergani S. D., Molinari E., Zerbi F. M., Chincarini G., 2004, A&A, 415, 171

Vergani S. D., et al., 2010, GRB Coordinates Network, 10495

Verner D. A., Ferland G. J., Korista K. T., Yakovlev D. G., 1996, ApJ, 465, 487

Vogelsberger M., et al., 2014a, MNRAS, 444, 1518

Vogelsberger M., et al., 2014b, Nature, 509, 177

Vreeswijk P., Jaunsen A., 2006, GRB Coordinates Network, 4974

Vreeswijk P., Jakobsson P., Ledoux C., Thoene C., Fynbo J., 2006, GRB Coordinates Network, 5535

Vreeswijk P. M., Jakobsson P., Jaunsen A. O., Oslo U., Ledoux C., 2008a, GRB Coordinates Network, 7391

Vreeswijk P. M., Thoene C. C., Malesani D., Fynbo J. P. U., Hjorth J., Jakobsson P., Tanvir N. R., Levan A. J., 2008b, GRB Coordinates Network, 7601

Vreeswijk P. M., Fynbo J. P. U., Malesani D., Hjorth J., de Ugarte Postigo A., 2008c, GRB Coordinates Network, 8191

Vreeswijk P., Malesani D., Fynbo J., Jakobsson P., Thoene C., Sollerman J., Watson D., Milvang-Jensen B., 2008d, GRB Coordinates Network, 8301

Vreeswijk P., Groot P., Carter P., Warwick U., Xu D., De Cia A., Jakobsson P., Fynbo J., 2011a, GRB Coordinates Network, 11640

Vreeswijk P., Fynbo J., Melandri A., 2011b, GRB Coordinates Network, 12648

Wang X.-G., et al., 2015, ApJS, 219, 9

Watson D., et al., 2013, ApJ, 768, 23

Wiersema K., et al., 2011, GRB Coordinates Network, 12431

Wiersema K., Vaduvescu O., Tanvir N., Levan A., Hartoog O., 2013, GRB Coordinates Network, 14617

Wilms J., Allen A., McCray R., 2000, ApJ, 542, 914

Woosley S. E., Bloom J. S., 2006, ARA&A, 44, 507

Xu D., Fynbo J. P. U., D'Elia V., Tanvir N. R., 2012, GRB Coordinates Network, 13460

Xu D., et al., 2013a, GRB Coordinates Network, 14273

Xu D., de Ugarte Postigo A., Schulze S., Jessen-Hansen J., Leloudas G., Kruehler T., Fynbo J. P. U., Jakobsson P., 2013b, GRB Coordinates Network, 14478

Xu D., et al., 2013c, GRB Coordinates Network, 14956

Xu D., Fynbo J. P. U., Jakobsson P., Cano Z., Milvang-Jensen B., Malesani D., de Ugarte Postigo A., Hayes M., 2013d, GRB Coordinates Network, 15407

Xu D., et al., 2013e, GRB Coordinates Network, 15451

Xu D., Vreeswijk P. M., Fynbo J. P. U., D'Elia V., Wiersema K., Tanvir N. R., de Ugarte Postigo A., Covino S., 2014, GRB Coordinates Network, 17040

Xu D., Tanvir N. R., Malesani D., Fynbo J., 2015a, GRB Coordinates Network, 18505

Xu D., Tanvir N. R., Malesani D., Fynbo J., 2015b, GRB Coordinates Network, 18506

Xu D., Tanvir N. R., Malesani D., Fynbo J. P. U., Jakobsson P., Saario J., 2015c, GRB Coordinates Network, 18696

Xu D., Xin L.-P., Wang J., 2016, GRB Coordinates Network, 18969

Younes G., Barthelmy S. D., 2012, GRB Coordinates Network, 13721

Yu H.-F., 2015, GRB Coordinates Network, 17579

Zhang B.-B., 2014a, GRB Coordinates Network, 15833

Zhang B.-B., 2014b, GRB Coordinates Network, 16798

Zhang B.-B., 2015, GRB Coordinates Network, 17674

Zhang J., Mao J., Bai J., 2015, GRB Coordinates Network, 18493

Zheng W., Filippenko A. V., Yuk H., Zhu Y., Perley D. A., 2015, GRB Coordinates Network, 18273

da Silva R., Fumagalli M., Worseck G., Prochaska X., 2011, GRB Coordinates Network, 11635

de Ugarte Postigo A., Tomasella L., 2015, GRB Coordinates Network, 17710

de Ugarte Postigo A., Gorosabel J., Fynbo J. P. U., Wiersema K., Tanvir N., 2009a, GRB Coordinates Network, 9771

de Ugarte Postigo A., et al., 2009b, GRB Coordinates Network, 10042

de Ugarte Postigo A., Thoene C. C., Vergani S. D., Milvang-Jensen B., Fynbo J., 2010, GRB Coordinates Network, 10445

de Ugarte Postigo A., et al., 2011a, GRB Coordinates Network, 11579

de Ugarte Postigo A., Castro-Tirado A. J., Tello J. C., Cabrera Lavers A., Reverte D., 2011b, GRB Coordinates Network, 11993

de Ugarte Postigo A., Thoene C. C., Gorosabel J., Sanchez-Ramirez R., Fynbo J. P. U., Tanvir N., Alvarez Iglesias C. A., 2013a, GRB Coordinates Network, 14380

de Ugarte Postigo A., Tanvir N., Sanchez-Ramirez R., Thoene C. C., Gorosabel J., Fynbo J. P. U., 2013b, GRB Coordinates Network, 14437

de Ugarte Postigo A., Xu D., Malesani D., Gorosabel J., Jakobsson P., Kajava J., 2013c, GRB Coordinates Network, 15187

de Ugarte Postigo A., Thoene C. C., Sanchez-Ramirez R., Gorosabel J., Fynbo J. P. U., Tanvir N. R., Alvarez Iglesias C. A., 2013d, GRB Coordinates Network, 15408

de Ugarte Postigo A., et al., 2014a, GRB Coordinates Network, 15924

de Ugarte Postigo A., et al., 2014b, GRB Coordinates Network, 16310

de Ugarte Postigo A., et al., 2014c, GRB Coordinates Network, 16902

de Ugarte Postigo A., Thoene C. C., Tanvir N. R., Gorosabel J., Fynbo J., Lombardi G., Reverte-Paya D., Perez D., 2014d, GRB Coordinates Network, 16968

de Ugarte Postigo A., Thoene C. C., Gorosabel J., Tanvir N., Fynbo J. P. U., Pesev P., Gomez Velarde G., Perez Valladares D., 2014e, GRB Coordinates Network, 17198

de Ugarte Postigo A., Kruehler T., Flores H., Fynbo J. P. U., 2015a, GRB Coordinates Network, 17523

de Ugarte Postigo A., et al., 2015b, GRB Coordinates Network, 17583

Table A1. Photon index Gaussian fits.

| Parameter	Mean	Standard deviation
Complete sample	1.95 ± 0.01	0.19 ± 0.01
Redshift sub-sample	1.93 ± 0.02	0.19 ± 0.01
SHOALS	1.95 ± 0.02	0.23 ± 0.02
low-mass sub-sample	1.95 ± 0.03	0.25 ± 0.02
high-mass sub-sample	1.98 ± 0.04	0.18 ± 0.04

de Ugarte Postigo A., Thoene C., Lombardi G., Perez A., 2015c, GRB Coordinates Network, 18274

de Ugarte Postigo A., Malesani D., Xu D., 2015d, GRB Coordinates Network, 18426

de Ugarte Postigo A., Pugliese G., Xu D., Malesani D., 2016a, GRB Coordinates Network, 18886

de Ugarte Postigo A., Thoene C. C., Sanchez-Ramirez R., 2016b, GRB Coordinates Network, 18966

van Dyk D. A., Connors A., Kashyap V. L., Siemiginowska A., 2001, ApJ, 548, 224

van der Marel R. P., 2006, in Livio M., Brown T. M., eds, The Local Group as an Astrophysical Laboratory. pp 47–71 (arXiv:astro-ph/0404192), http://adsabs.harvard.edu/cgi-bin/nph-data_query?bibcode=2009IAUS..256...81V&link_type=ARTICLE&db_key=AST&high=

van der Marel R. P., Kallivayalil N., Besla G., 2009, in Van Loon J. T., Oliveira J. M., eds, IAU Symposium Vol. 256, The Magellanic System: Stars, Gas, and Galaxies. pp 81–92 (arXiv:0809.4268), doi:10.1017/S1743921308028299

von Kienlin A., 2010, GRB Coordinates Network, 11015

von Kienlin A., 2014a, GRB Coordinates Network, 15790

von Kienlin A., 2014b, GRB Coordinates Network, 16152

von Kienlin A., et al., 2014, ApJS, 211, 13

APPENDIX A: PHOTON INDEX DISTRIBUTION

For completeness, we report the intrinsic photon index distribution of GRB afterglows, which is a side-products of our analysis. The X-ray spectrum of the complete sample was analysed to obtain constraints on the slope of the intrinsic powerlaw. The constraints for the complete sample is shown in Figure A1. We approximate the distribution by a Gaussian distribution, plotted in red. The overall distribution is centred at $\Gamma = 1.94$ with a width of $\sigma = 0.20$. Table A1 shows the mean and standard deviations obtained from the various samples. The Gaussian distribution provides a good approximation in the bulk of the population. However the data show heavier tails, including $\Gamma < 1.5$ and $\Gamma > 2.4$. The individual spectra show no obvious signs of bad fits in either extreme. The high-mass subsample and redshift subsample show steeper slopes with a narrower distribution, but the difference is smaller than the uncertainties.

Curran et al. (2010) investigate the photon index distribution based on the automatic fitting results of Evans et al. (2009) of 301 GRBs. They find a peak at $\Gamma \approx 2.1$, and the distribution spreads the full range of $1 - 3$. In contrast, we find that the standard deviation of the distribution is much narrower ($\sigma = 0.2$) than their analysis suggests ($\sigma \approx 0.5$). This is probably because of their use of best-fit values, which introduce additional scatter, and the fact that the completely automated analysis of Evans et al. (2009) sometimes chooses time windows affected by prompt emission while we manually verified each time window. Wang et al. (2015) performed temporally resolved fitting of X-ray and optical data and found $\Gamma = 1.98$ with standard deviation $\sigma = 0.15$, which is consistent with our results.
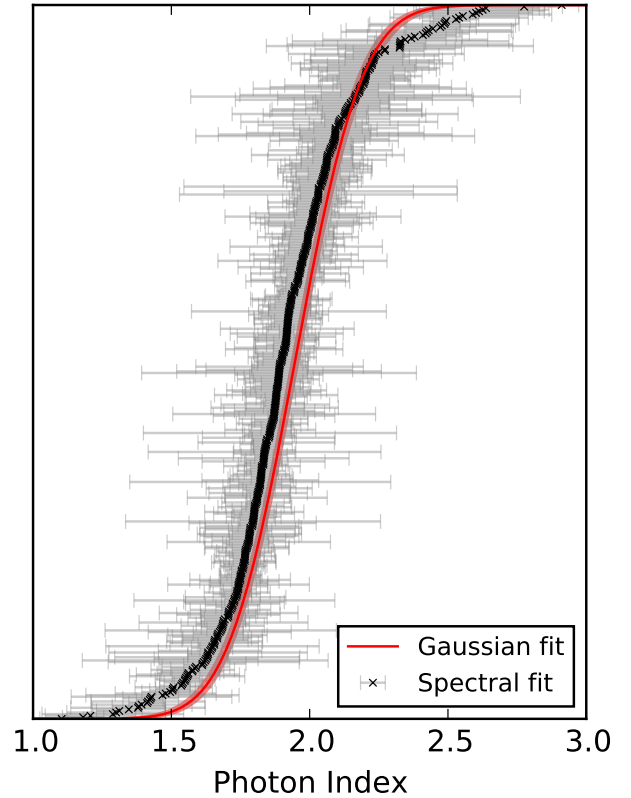
Figure A1. Caterpillar plot of the photon index. Constraints on the photon index of the intrinsic powerlaw are shown as error bars for each object, sorted by their mean. During the population analysis we assumed a Gaussian for the distribution of photon indices (red). The spectral index β is related to the photon index as $\beta = \Gamma - 1$.

Curran et al. (2010) then considers two regimes in which synchrotron radiation is produced: (a) The electron energy distribution index p relates to the spectral index ($\beta = \Gamma - 1$) as $p = 2 \cdot \beta$ when the cooling frequency is below the X-ray frequency ($\nu_c < \nu_X$), and (b) as $p = 2 \cdot \beta + 1$ otherwise ($\beta = (p[-1])/2 + 1$. Adopting a Gaussian distribution for p centred at, e.g., 2.2 then yields a double-peaked distribution for the photon index centred at $\Gamma = 2.1$, with a secondary, small component (case b) offset by 0.5. Here, we find additional contributions at both lower and higher photon indices which necessitate a different model than two Gaussian peaks, and we can therefore not unambiguously conclude that $\nu_c > \nu_X$ applies in most cases. Nevertheless, if that is assumed, we find $p = 2$ for the electron density distribution index distribution with a standard deviation of 0.4.

APPENDIX B: X-RAY BACKGROUND MODEL

The shape of the XRT background has been analysed by Pagani et al. (2007) (see Figure 2 there). It shows a steep increase below 0.5 keV and several bumps. The background spectra analysed in this work show the same shape. We fit the background spectrum with a broken powerlaw model and four Gaussian components at ∼ 0.7, 2.2, 1.2 and 0.4 keV, by order of importance. The parameters of this model are optimised according to the Poisson likelihood. In further analysis, the background model parameters are held fixed, and the background model is added to the source spectral fit, scaled

by the area ratio of the spectral extraction regions. Our code and model for fitting the *Swift*/XRT background is available as part of the BXA software.

APPENDIX C: NUMERICAL DETAILS ON FITTING THE ELLIPSOIDS MODELS

This section describes how the SingleEllipsoid model is computed. Monte Carlo ray-tracing simulations are used to compute the column density distribution $p(N_H|M, \theta)$.

First, random points inside the ellipsoid are generated. The ellipsoids equation,

$$\left(\frac{p_x}{r_x}\right)^2 + \left(\frac{p_y}{r_y}\right)^2 + \left(\frac{p_z}{r_z}\right)^2 \leq 1, \tag{C1}$$

describes whether a point $\mathbf{p} = (p_x, p_y, p_z)$ is inside. The radii are $r_x = r_y = R$ and $r_z = z$ under cylindrical symmetry. For constant density sampling, (p_x, p_y, p_z) are first drawn uniformly in $p_x \sim U(-R, R)$, $p_y \sim U(-R, R)$, $p_z \sim U(-z, z)$ and the vector $\mathbf{p}$ is rejected if outside the ellipsoid.

Second, a random unit direction vector is generated. Three unit normal variates are combined to a vector $\mathbf{d} \sim (N(0, 1), N(0, 1), N(0, 1))$ which is then normalised to unit length $\mathbf{n} = \mathbf{d}/|\mathbf{d}|$.

Third, the length l of the ray inside the ellipsoid needs to be computed, which is the distance between $\mathbf{p}$ and the point where the ray exits the ellipsoid, $\mathbf{q}$. The coordinates of $\mathbf{q}$ are governed by Equation C1 and the line equation,

$$\mathbf{q} = \mathbf{p} + l \cdot \mathbf{n}, \tag{C2}$$

which yield the quadratic equation

$$\left(\frac{p_x + l \cdot n_x}{r_x}\right)^2 + \left(\frac{p_y + l \cdot n_y}{r_y}\right)^2 + \left(\frac{p_z + l \cdot n_z}{r_z}\right)^2 = 1 \tag{C3}$$

with l unknown. Equation C3 has two solutions for l (one for the positive, one for the negative direction). Only the positive one is considered. With

$$b = \frac{p_x \cdot n_x}{r_x^2} + \frac{p_y \cdot n_y}{r_y^2} + \frac{p_z \cdot n_z}{r_z^2} \tag{C4}$$

$$a = \frac{n_x^2}{r_x^2} + \frac{n_y^2}{r_y^2} + \frac{n_z^2}{r_z^2} \tag{C5}$$

$$c = \frac{p_x^2}{r_x^2} + \frac{p_y^2}{r_y^2} + \frac{p_z^2}{r_z^2} \tag{C6}$$

$$d = b^2 - a \cdot c \tag{C7}$$

$$l = \begin{cases} 0 & \text{if } d < 0 \\ (-b + \sqrt{d})/a & \text{otherwise} \end{cases}, \tag{C8}$$

we can finally write the column probed by the ray as $N_H = N_H^{major} \cdot l$, where N_H^{major} is the column density of the ellipsoid in a unit length. The problem is fundamentally degenerate (N_H^{major} and size), so $R = 1$ is assumed for the SingleEllipse model.

To compute the column density distribution, $p(N_H|M, \theta)$, 400000 random rays are generated. A histogram of their N_H between $10^{19} - 10^{26}$cm^{-2} with 100 logarithmically spaced bins provides a well-sampled approximation. A problem may occur with less obscured column densities in the simulation, which can

never be measured due to Milky Way absorption. For simplicity, the column density of each ray is modified as $N_H' = N_H + 10^u$ with the random number $u \sim U(19, 20)$ to ensure all rays have $N_H > 10^{19}$cm^{-2}. This redistributes unobscured rays to the range $10^{19} - 10^{20}$cm^{-2}, uniformly, and, although done primarily for numerical reasons, may be interpreted as placing the ellipsoid in a low-density gas with $N_H < 10^{20}$cm^{-2}.

The arising distribution (see Figure 6) cannot be approximated by simple analytic formulas. Towards low N_H values, the distribution rises exponentially. For very low z/R ratios, the distribution declines exponentially toward high N_H values, but the peak is too wide/narrow to be fitted by a broken/bending powerlaw. Additionally, for moderate z/R ratios, there is a steep truncation at $N_H = 2$ (see Figure 6) which declines faster than a exponential cut-off.

To emulate a dispersion in the population of $\log N_H^{major}$ of standard deviation σ, the histogram is convolved with a Gaussian. Finally, linear interpolation of the histogram is used to evaluate $p(N_H|M, \theta)$ at arbitrary N_H values.

The MultiEllipsoid model generates points proportional to the mass in each ellipsoid, which is

$$M \propto N_H^{major} \cdot r_x \cdot r_y \cdot r_z$$

The ellipsoid to draw from is chosen randomly in proportion to its masses M. Rays now may probe multiple ellipsoids, and the final N_H is the sum of all ellipsoids encountered. The definition of l has to be modified because some rays may not originate inside the ellipsoid at hand (checked with Equation C1), but cross it. In that case the distance l is between the two quadratic solutions, giving

$$l_{cross} = 2 \cdot \sqrt{d}/a.$$

Otherwise, the same procedure as in the SingleEllipsoid model is applied.

To simulate the column density from the centre, $\mathbf{p} = (0, 0, 0)$ is set fixed, and the procedure of generating random rays is applied in the same fashion.

This paper has been typeset from a TEX/LATEX file prepared by the author.